MHz Free electron laser X-ray diffraction and Modelling of pulsed laser heated diamond anvil cell

Nicolas Jaisle,[1] David Cébron,[1] Zuzana Konôpková,[2] Rachel J Husband,[3] Clemens Prescher,[4] Valerio Cerantola,[2] Anand Dwivedi,[2] Johannes M. Kaa,[5] Karen Appel,[2] Khachiwan Buakor,[2] Orianna B. Ball,[6] Ryan S. McWilliams,[6] Cornelius Strohm,[3] Motoaki Nakatsutsumi,[2] Ulf Zastrau,[2] Carsten Baehtz,[2] Marzena Anna Baron,[7] Eric Edmund,[8] Joydipa Biswas,[4] James D. McHardy,[6] Blake T. Sturtevant,[9] Lars Ehm,[10] Alexander F. Goncharov,[8] Malcolm I. McMahon,[6] Johannes Buchen,[11] Hyunchae Cynn,[12] Edward J. Pace,[6] Hanns-Peter Liermann,[3] Daniel T. Sneed,[12] Samantha C. Cooper,[9] Madison Anae,[10] Jaeyong Kim,[13] Zhongyan Wu,[13] Yongjae Lee,[14] Huijeong J. Hwang,[14] Taehyun Kim,[14] Jinhyuk Choi,[14] Jeongmin Lee,[14] Sébastien Merkel,[7] Julien Chantel,[7] Egor G. Koemets,[11] Hauke Marquardt,[11] Vitali B. Prakapenka,[15] Stella Chariton,[15] Elena Shevchenko,[15] Guillaume Fiquet,[16] Angelika D. Rosa,[17] Mohamed Mezouar,[17] Gaston Garbarino,[17] and Guillaume Morard[1]

[1)] *Univ. Grenoble Alpes, Univ. Savoie Mont Blanc, CNRS, IRD, Univ. Gustave Eiffel, ISTerre, 38000 Grenoble, France*

[2)] *European XFEL GmbH, Holzkoppel 4, Schenefeld, Germany*

[3)] *DESY Deutsches Elektronen-Synchrotron, Notkestr. 85, Hamburg, Germany*

[4)] *Institute of Earth and Environmental Sciences, Albert-Ludwigs University of Freiburg, Freiburg, Germany*

[5)] *Tech. Univ. Dortmund Fakultät Physik/DELTA, Maria-Goeppert-Mayer-Straße 2, 44227 Dortmund, Germany*

[6)] *School of Physics and Astronomy, University of Edinburgh, Edinburgh, United Kingdom*

[7)] *Univ. Lille, CNRS, INRAE, Centrale Lille, UMR 8207 - UMET - Unité Matériaux et Transformations, F-59000 Lille, France*

[8)] *Earth and Planets Laboratory, Carnegie Institution for Science, Washington, DC 20015, USA*

[9)] *Los Alamos National Laboratory, Los Alamos 87545, USA*

[10)] *Dpt. of Geosciences, Stony Brook University, 255 Earth and Space Sciences Building, Stony Brook, New York 11794, USA*

[11)] *Dpt. of Earth Sciences, University of Oxford, Oxford OX1 3AN, United Kingdom*

[12)] *Lawrence Livermore National Laboratory, Livermore 94550, USA*

[13)] *Dpt. of Physics, Hanyang University, Haengdang dong, Seoul, South Korea*

[14)] *Yonsei University, Department of Earth System Sciences, Republic of Korea*

[15)] *University of Chicago, CNM, ANL, Chicago 60637, USA*

[16)] *Institut Minéralogie, de Physique des Matériaux et de Cosmochimie, Sorbonne Univ., 4 Place Jussieu, Paris, France*

[17)] *European Synchrotron Radiation Facility, Grenoble, France*

(*guillaume.morard@univ-grenoble-alpes.fr)

(*david.cebron@univ-grenoble-alpes.fr)

(*nicolas.jaisle@univ-grenoble-alpes.fr)

(Dated: 16 October 2023)

A new diamond anvil cell experimental approach has been implemented at the European X-ray Free Electron Laser, combining pulsed laser heating with MHz X-ray diffraction. Here we use this setup to determine liquidus temperatures under extreme conditions, based on the determination of time resolved crystallization. The focus is on a Fe-Si-O ternary system, relevant for planetary cores. This time-resolved diagnostic is complemented by a finite element model, reproducing temporal temperature profiles measured experimentally using streaked optical pyrometry. This model calculates the temperature and strain fields by including (i) pressure and temperature dependencies of material properties, and (ii) the heat-induced thermal stress, including feedback effect on material parameter variations. Making our model more realistic, these improvements are critical as they give 7000 K temperature differences compared to previous models. Laser intensities are determined by seeking minimal deviation between measured and modeled temperatures. Combining models and streak optical pyrometry data extends temperature determination below detection limit. The presented approach can be used to infer the liquidus temperature by the appearance of SiO_2 diffraction spots. In addition, temperatures obtained by the model agree with crystallization temperatures reported for Fe-Si alloys. Our model reproduces the planetary relevant experimental conditions, providing temperature, pressure and volume conditions. Those predictions are then used to determine liquidus temperatures at experimental timescales where chemical migration is limited. This synergy of novel time-resolved experiments and finite-element modeling pushes further the interpretation capabilities in diamond anvil cell experiments.

I. INTRODUCTION

Determination of incongruent (i.e. partial) melting in geomaterials is crucial to understand planetary evolution, from the early differentiation during the magma ocean stage to crys-

tallization of planetary cores and the heat budget of planetary dynamos[1,2]. Laser-heated diamond anvil cell (LH-DAC) experiments combined with X-ray diffraction (XRD) are a commonly used method to probe partial melting under high pressure and high temperature conditions. However, it remains challenging for LH-DAC experiments using conventional methods to accurately resolve liquidus temperatures due to chemical migration during the experiments. Therefore, results from melting experiments using LH-DAC can exhibit large discrepancies between each other[3–5]. Different chemical migration processes were suggested to explain those discrepancies including carbon contamination[6] (Fig. 1).

One key feature of this chemical migration is the resulting difference between the composition of the initial sample and the composition of the liquid probed at high temperature.

Indeed one of the most problematic issues related to temperature gradients is the consequent chemical migration inside the sample (Fig. 1). Chemical migration is observed in the solid state[7,8] or related to partial melting[9,10]. Different phenomena are suggested to explain this chemical migration in the presence of temperature gradients. Among those, one of the most discussed is the Soret effect[7,11]. In addition, the surface tension[12] as well as the convection upon melting[13] could cause chemical migration inside the partially molten sample. All these effects induce a chemical gradient between the hot and cold part of the sample, with the probed area then having a different composition from the initial bulk one.

In order to minimize this chemical migration, a new experimental approach has been developed, combining time-resolved X-ray diffraction and pulse laser heating. The MHz pulse train structure of the European X-ray Free Electron Laser (EuXFEL) is particularly suited to study partial melting as it allows for time-resolved X-ray diffraction where each X-ray pulse is spaced hundreds of nanoseconds apart. Microsecond heating and cooling timescales are sufficiently short to suppress chemical migration during event, and the high X-ray intensities at EuXFEL provide diffraction patterns with a high signal-to-noise ratio[14].

Experiments were performed at EuXFEL at 2.257 MHz X-ray pulse frequency (one pulse every 443 ns), with XRD acquired by an Adaptive Gain Integrating Pixel Detector (AGIPD) 500k, capable of acquiring separately each pulse. Upon each pulse train, streaked optical pyrometry (SOP) measurements were collected in order to obtain surface temperature data along with the XRD data. To be more finely constrained, temperature analysis and XRD data are complemented by numerical modelling, which is done with the Finite Element Method (FEM) using the COMSOL commercial software[15]. FEM can provide constraints on the temperature distribution inside the sample, the temperature gradients throughout the heating event, as well as evaluate the thermal stress. Differences between simple parametric temperature estimates in the pressure medium[16] and FEM model results[17] highlight their importance for LH-DAC experiments.

The presented experiment is focused on probing the Fe-Si-O ternary phase diagram, Si and O being two possible major light elements in the Earth's liquid outer core[18]. Fe-Si-O moreover represents an archetypal example of chemical migration in LH-DAC[9]. The aim of the experiment is to describe the liquidus temperature observed by the SiO_2 recrystallization, as well as to benchmark our SOP measurements and FEM model following the well constrained Fe-Si solidification temperatures of Fe-Si alloys.

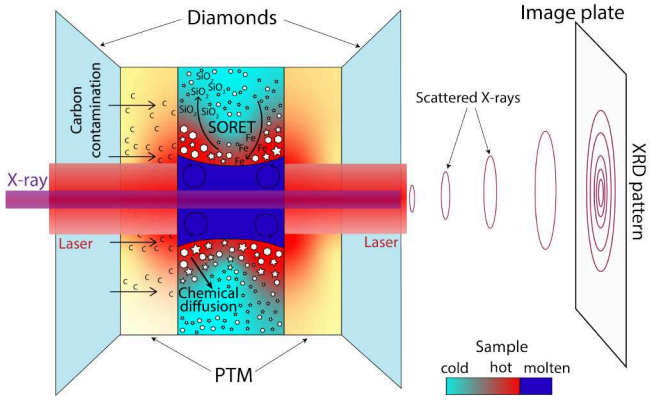

FIG. 1. Schematic representation of potential biases in laser heated diamond anvil cell experiments (not to scale). PTM stands for pressure transmitting medium. Temperature gradients inherent to laser heating might lead to i) Carbon diffusion from the diamond anvil, leading to sample contamination, ii) convection inside the molten sample leading to enhanced chemical interaction at the solid-liquid interface, iii) Soret diffusion[7,11] leading *a priori* to transfer of lighter elements towards hot zone and heavier elements towards cold zone as observed in FeSiO alloys[9]. iv) other forms of chemical diffusion, possibly leading to compositional gradient. The mineralogical assemblage probed by XRD and used to infer phase melting might therefore not correspond to the pristine sample compositions.

For the first time in LH-DAC experiments, the Fe-Si-O ternary system liquidus temperature could be measured under high pressure owing to the strong chemical migration of Fe and SiO2 under standard experimental conditions.

In this paper, an overview of the experimental LH-DAC setup is first provided in section II, together with the methods used for sample heating, XRD analysis achieved at the EuXFEL, and *post-mortem* analysis. Then, the section III describes our FEM model, reproducing the experimental conditions by using laboratory SOP values and detailed material parameters taking into account heat transfer and thermal pressure. Results and model output are presented in section IV after adjustment with the data. That section underlines how models can enhance available temperature data and XRD interpretation. The presented models are also compared to previous work in order to highlight improvements in precision and interpretation of experimental data. Section V concludes with some suggestion of future model improvements.

II. METHODS

Experiments were performed at the High Energy Density (HED) instrument[19] at the EuXFEL using the dedicated DAC set-up in interaction chamber 2 (IC2)[14,20]. For our experiment (# 2605), we used symmetric cells[21] equipped with Boehler-

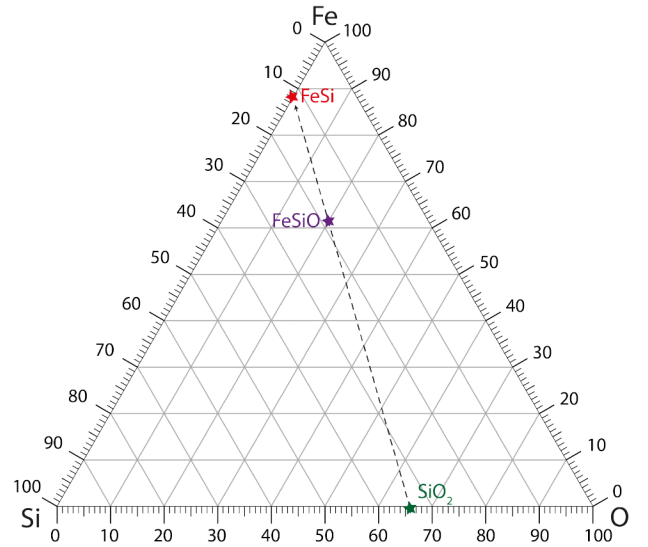

	Atomic %	Wt %
FeSiO	61.1% Fe-18.9% Si-20% O	80.2% Fe-12.35% Si-7.45% O
SiO_2	66.7% O - 33.3% Si	46.67% Si-53.33% O
FeSi	12.5% Si-87.5% Fe	7% Si-93% Fe

FIG. 2. Demixing line of the ternary Fe-Si-O system. The purple point highlights the initial FeSiO alloy composition used during our experiment. The dashed arrow represents the chemical pathway followed by the sample as it cools down. This allows inferring the formation of SiO_2 (lower right green star) out of the initial alloy (purple star) until only pure FeSi remains (upper left red star). The final Fe-Si ratio in the formed Fe-Si alloy (around 7 wt% Si) is thus controlled by the initial composition.

Almax conical support and diamond[22] with a large aperture of 70° on the opposite side of X-ray arrival direction (downstream), suited to access a wide diffraction angular range, and a standard diamond on X-ray arrival side (upstream). The sample chamber drilled in a Re gasket pre-indented to 50 µm was loaded with an assembly of two KCl disks (diameter 120 µm and thickness of 20 µm) surrounding an Fe-Si-O alloy sample (Fig. 2) with a diameter of approximately 60 µm and 9.2 µm thickness. This alloy consists of 80.2 wt% Fe, 12.35 wt% Si and 7.45 wt% O measured by electron microprobe and was synthesized by plasma vapor deposition (PVD) (Dephis company)[9].

KCl was chosen as pressure transmitting medium (PTM) because it is not considered to react with iron[3,24] in addition to its good thermal insulation. In addition, the KCl can be used as an internal diffraction standard by monitoring the XRD peak shift (and thus lattice volume change) related to pressure by its equation of state (EoS)[25]. After loading, the entire cell is kept inside a vacuum oven at 120°C in order to ensure dehydration and thus absence of water inside the sample chamber. The pressure on the sample was increased by tightening the screws and measured using the KCl XRD.

The experiment was performed inside interaction chamber 2 (IC2) using the DAC platform[14,26]. High sample temperatures were generated using double sided, on-axis, pulsed laser heating (SPI G4 laser with $\lambda = 1070$ nm) with a 250 ns pulse length.

The laser is coming from a single source which is split into two beams before being injected in the optical path by dichroïc mirrors and brought to the sample's surface by a series of optical components[26]. Incoming laser intensity on the sample's surface can be controlled by the polarizing beam splitting cubes (polarizers) and rotating waveplates in each laser beampath, going upstream and downstream of the DAC. The Gaussian shaped laser focal spot size was $12-13$ µm full width at half maximum (FWHM) (measured with a Thorlabs optical beam profiler).

Based on the prediction of the alloy's corresponding ternary phase diagram (Fig. 2), the formation of SiO_2 and FeSi are expected upon sufficiently high laser heating (typically above SiO_2 melting temperature around 4000-5000 K). To achieve this, we use a single laser pulse in order to limit heating duration below the microsecond and keep the composition as close as possible to the initial one in order to follow the expected chemical pathway (i.e. to perform the experiment faster than any chemical migration might happen).

SOP data was collected in spectral mode[27] using a Hamamatsu streak camera with a S-20 photocathode coupled to a Princeton Instrument spectrometer to acquire the optical surface emission on the downstream side[26]. The camera's sweep window was set to 5 µs. Calibration was done with a tungsten incandescence standard lamp used as a thermal source with a known temperature of 2900 K.

Temperature measurement using a streak camera is essential for the short timing of the present experiment (5 µs), however the drawback is a reduced sensitivity. Only temperature measurements above 4000 K were reliable here, requiring an extrapolation to longer timescales and lower temperatures.

The experiment was performed using a photon energy of 18 keV ($\lambda = 0.6968$ Å) producing high-brilliance pulse trains (about 10^{10} photons per pulse)[20]. In agreement with the expected sample cooling duration after a laser pulse, data were collected using a pulse train with up to 40 pulses with a 443 ns separation (2.257 MHz repetition rate) that totals 17.277 µs. Due to the nature of self-amplified spontaneous emission (SASE) of a FEL, the relative intensities of the pulses inside a train can fluctuate and were measured for each train[20]. The X-ray beam was focused using a series of compound refractive lenses (CRLs) to a diameter below 10 µm, smaller than the laser spot size to ensure probing a homogeneous temperature distribution. Attenuators are used along the beam path to limit X-ray intensity which can otherwise be high enough to induce heating as demonstrated by previous experiments[28,29] and could heat on top of laser (up to 10000 K for Fe sample[28,29]). The experiments presented in this study were performed with the aim of keeping X-ray heating to a minimum. To ensure this experimentally, we performed preliminary runs in order to assess the amount of X-ray transmission needed to generate detectable heating due to X-ray alone (with optical laser off). Heating was quantified by the sample's main diffraction peak shifting within a pulse train. The absence of X-ray heating in the data was checked as well by varying X-ray intensity model input and is explained more in detail in the first section of the supplementary material.

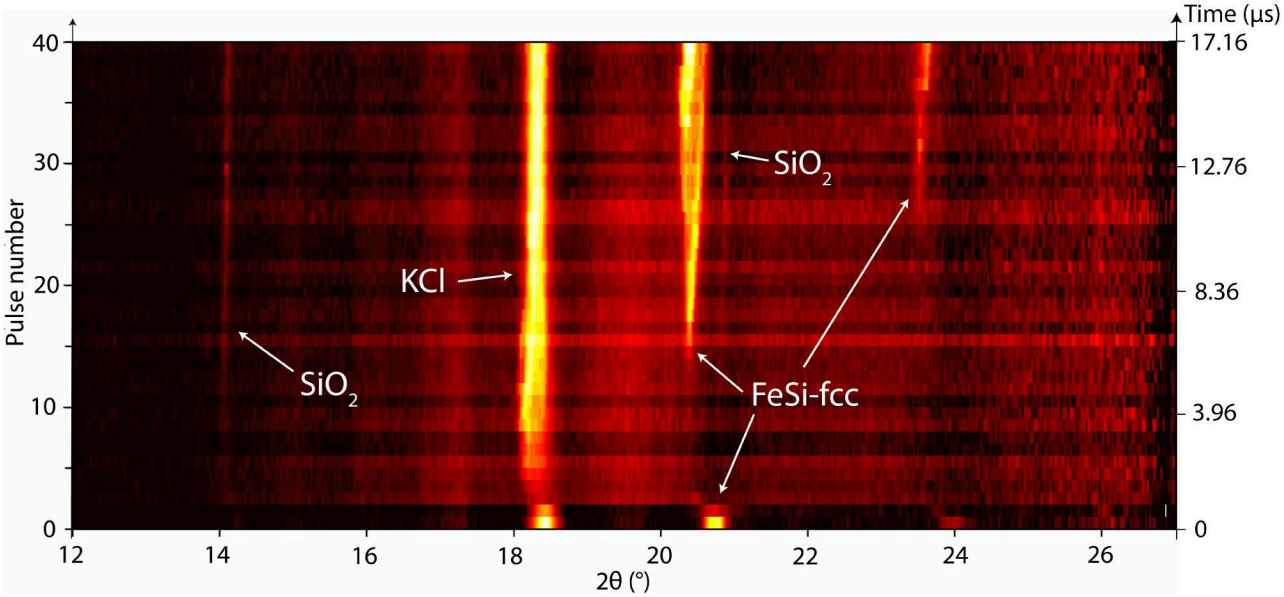

FIG. 3. Batch view of pulse train diffraction spectra series[23]. The pulse frequency was 2.257 MHz (time range span of 17.16 µs for 40 pulses). The moments where phases are first observed (spawn times) can be constrained by seeking the line apparition and checking for spots on the image plate. Observable phases are highlighted and designated. The KCl peak partly fades over the first pulses where the maximum fiber laser intensity is delivered to the sample, meaning that it is likely almost entirely molten inside the X-ray sampling zone. The first sample phase to crystallize upon cooling is SiO_2. It is observed for the first time on the diffraction spectra at 2.2 µs (time zero corresponding to the first X-ray pulse). The FeSi-fcc peaks entirely disappear within the first 3 pulses before re-appearing at 5.72 µs for the left peak. Note that the second and fainter higher angle peaks of FeSi-fcc and SiO_2 appear later in time, likely due to signal degradation at higher angles and large crystal size.

Once the X-ray heating was minimized, the sample was moved to an unheated position. On this fresh spot, a YAG laser pulse was applied simultaneously to the attenuated X-ray pulse train. Spatial alignment between laser and X-ray was verified before the shot. The sample was laser heated in different locations (see diffraction map in supplementary material). The adjustable delay between the X-ray and laser pulse was set to synchronize heating and probing; starting the laser and X-ray pulse train nearly simultaneously. The delay between pump and probe was set so that the first acquired X-ray pulse provides a diffraction pattern of the bulk sample at ambient temperature. Note that the SOP acquisition is shifted compared to this starting moment and its acquisition starts 0.521 µs earlier than the laser pulse and 0.22 µs earlier than the first X-ray. The laser heating pulse intensity was raised stepwise, up to the value where a complete melting and crystallization sequence was observed in the XRD data at different sample positions. Our analysis focuses on one run where the heating produced full melting.

Pulse-resolved XRD data were collected with an AGIPD[30,31] at the intra-train repetition rate of the XFEL pulse train (2.257 MHz). AGIPD was positioned outside of the vacuum chamber. The sample-to-detector distance (422.3 mm), detector tilt and rotation were calibrated using CeO_2 diffraction standard in the DIOPTAS software[23]. Diffraction images were radially integrated using DIOPTAS to produce 1D diffraction profiles for the image sequence of the complete train plotted against 2Θ (see Fig.3).

For complementary *ex-situ* observations and measurements under scanning electron microscopy (SEM), the sample was cut using a focused ion beam (FIB) at the EuXFEL (Appendix B). Relative composition analysis of heated vs non-heated sample was achieved with energy-dispersive X-ray spectroscopy (EDS).

III. FINITE ELEMENT MODEL

Finite element modeling gives access to certain measurements which are not available in DAC experiments, and allow temporal interpolation of the experimental data[13,28,32]. Here, the temperature field is calculated, extending on many aspects of previous COMSOL finite element models[28,33] (Figure 5). In particular the present model (i) includes the various EoS of the materials involved in our experiments, as well as their influence on the pressure induced geometry deformations, (ii) includes temperature and pressure dependencies of the parameters, (iii) combines laser and X-ray thermal heating, and (iv) takes into account the feedback of the thermal stress[34,35]. We highlight the differences to previous models in Figure 5. As the temperatures reached in this work are high enough to melt materials in our experiments, possible liquid flows have been tested on the model, following previous works[13]. However the effect of heat transfer due to fluid flow[13] has been neglected in the present computations.

Using the cylindrical coordinates (r, z), the geometry of our axisymmetric DAC numerical model is sketched in figure 4 and the geometrical parameters are given in Table I (full ge-

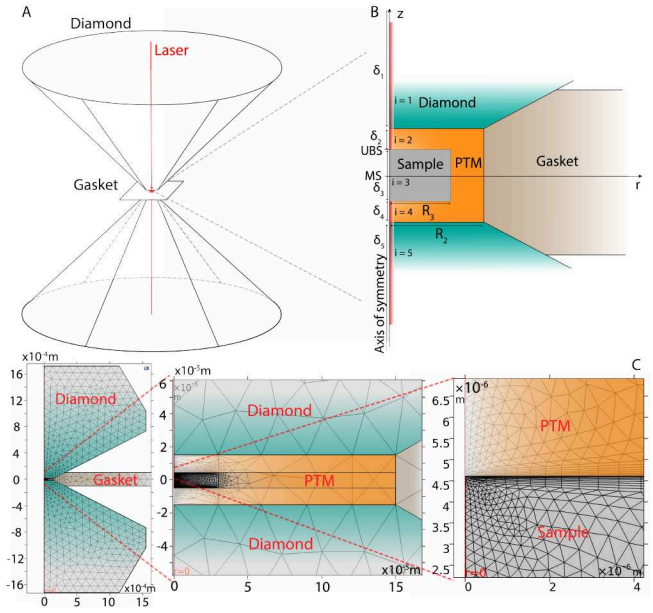

FIG. 4. A) Schematic of the DAC setup used in our numerical model. B) Zoom on our FEM 2D-axisymmetric geometry (not to scale), z-axis being the axis of symmetry in the cylindrical coordinates (r,z). Each domain has its specific properties (density, thermal conductivity, heat capacity...). UBS stands for upper border of the sample and MS for middle of the sample. C) Actual mesh example used in the simulation. Mesh is more finely constrained towards important boundaries (PTM/sample)

Medium	Radius R_i (μm)	Thickness δ_i (μm)
Diamond (i = 1,5)	1550	1720
PTM (i = 2,4)	30	8 | 4.983[a]
Sample (i = 3)	40	5.5 | 4.345[a]
Gasket	1500	$\delta_3 + 2\delta_2$

[a] $P_{ref} = 0$ | $P_{ref} = 61.9$ GPa

TABLE I. Geometric parameters of the COMSOL model. Following figure 4, the different media are numbered (i = 1: upper diamond, i = 2: upper PTM, etc.). We fix δ_3 at $P_{ref} = 0$ to be the sample's thickness observed on the FIB cut (that is $\delta_3 = 5.5$ μm for the studied run (#414), but it changes from run to run). The detailed geometry is provided in supplementary material.

ometry description is provided in supplementary material). Note that the initial pressure P_{ref} imposed on the DAC leads to important initial geometry deformations, which have to be taken into account. Having first calculated the complete (initial) elastic deformations of the geometry, our preliminary tests show that the various mechanical contacts between the different media raise several numerical issues if the various domains are not assumed to be glued (e.g. domains separation). As a first step, the model used here only accounts for the relevant leading order effects by simply changing the various media thicknesses in the model, using the material EoS of each medium (our model is detailed in Appendix C).

Our extended numerical DAC model aims at providing the temperature distribution under the total time-varying pressure $P_{ref} + P_{th}$, where the (*a priori* non-uniform) pressure P_{th} is related to thermal stress effects (pressure induced variations of the material parameters due to thermal expansion and boundary constraints). By contrast with previous models[13,28], this requires integrating the elastic equations together with the heat transfer equation. Considering quasi-static infinitely small displacements (negligible inertia), the stress tensor $\boldsymbol{\sigma}$ and the temperature T are governed by

$$\rho C_P \frac{\partial T}{\partial t} + \boldsymbol{\nabla} \cdot \boldsymbol{q} = Q, \tag{1}$$

$$\boldsymbol{\nabla} \cdot \boldsymbol{\sigma} = 0, \tag{2}$$

where the heat flux vector $\boldsymbol{q} = -k_{th}\boldsymbol{\nabla} T$ is given by Fourier's law, with the volume heat source Q (e.g. due to radiation absorption, as detailed in section C 2), and where all the physical parameters (ρ, C_P, k_{th}) of equation (1) depend *a priori* on space via their pressure and temperature dependencies (ρ being the material density, C_P the heat capacity at constant pressure, and k_{th} the thermal conductivity). However, these dependencies are generally not known and the material parameters have thus been taken as constant except for the KCl PTM density, and for the parameters (ρ, C_P, k_{th}) of the sample (see Table II). The boundary conditions and initial state used in our model to integrate equations (1)-(2) are provided in the appendix C 3.

Due to sparse literature on FeSiO material properties and its high Fe content, the sample parameters (including density) have been assumed to be similar to pure Fe (i.e. sample has properties of iron in the model). As simulations are generally performed at high pressures ($50 - 100$ GPa), only the high pressure, high temperature phases [ε-iron[36] (hcp), γ-iron[37] (fcc) and liquid Fe[38]] EoS were considered, where liquid Fe EoS employs a recently developed method to characterize the structure of liquids under high pressures as described in Morard et al. 2013[39]. Similarly for KCl, only the EoS of the B2-KCl[25] (high pressure phase) was considered. To obtain the density from EoS at a given temperature and pressure (T, P), we have used the EoS to calculate ρ on a large (T, P) range and the value used by our numerical model at each time step is then obtained by a 2D interpolation. When the needed values were out of the EoS validity range, as e.g. liquid Fe at very high temperatures, the density was assumed constant and equal to the closest value inside the validity range.

The pressure and temperature dependencies of k_{th} for the sample are obtained from the literature (Table II). This value predominantly controls the temperature field evolution (i.e. axial, radial), as well as the temperature decay rate. The C_P dependencies are more difficult to obtain, for instance for the hcp phase of iron. Here, C_P of the fcc phase of iron is obtained by combining thermodynamic relations (Appendix C); these expressions being also used (beyond their validity regime) to provide C_P estimates for the hcp phase of iron. Regarding C_P, the value effectively used in our numerical model is also affected by the latent heat of possible phase changes. The high temperatures reached in our experiments can indeed melt the materials, and phase change effects have thus to be taken into account. To do so, the apparent heat capacity method (AHCM) is used (Appendix C), and the values of C_P and k_{th}

are modified when phase changes occur (our model only considers AHCM for liquid-solid phase changes).

To integrate equation (2), a material rheology has to be chosen. A recent study highlights that non-isotropic deformation have an impact on pressure medium and sample final thickness, and therefore on later conductivity measurements in LH-DAC[49]. Reproducing this non-isotropic deformation yet demands more evolved models and we chose not to include it in this model. Here, the materials are all assumed to follow the usual Hooke's law for isotropic materials. Noting the elastic displacement $\boldsymbol{u}$, this law relates $\boldsymbol{\sigma}$ to the (infinitesimal) strain tensor $\boldsymbol{\epsilon} = [\nabla \boldsymbol{u} + (\nabla \boldsymbol{u})^{\top}]/2$ by

$$\boldsymbol{\sigma} = K\left[\mathrm{Tr}(\boldsymbol{\epsilon}) - \alpha_V (T - T_{ref})\right]\boldsymbol{I} + 2G\,\mathrm{dev}(\boldsymbol{\epsilon}), \qquad (3)$$

with the bulk modulus K, the identity matrix $\boldsymbol{I}$, the shear modulus G (with $G = 0$ in liquid domains), and the deviatoric strain tensor (or shear tensor) defined by $\mathrm{dev}(\boldsymbol{\epsilon}) = \boldsymbol{\epsilon} - \mathrm{Tr}(\boldsymbol{\epsilon})\boldsymbol{I}/3$. The total pressure $P_{ref} + P_{th}$ is then obtained by adding the thermal pressure $P_{th} = -\mathrm{Tr}(\boldsymbol{\sigma})/3$, which is *a priori* non-uniform in the domain. Equations (1) and (2) are thus coupled both ways: thermal stresses are generated by the T variations in equation (2) while the associated thermal pressure P_{th} modifies the physical parameters (ρ, C_P, k_{th}) in equation (1), e.g. for the sample in this experiment. Note that, while our model provides the stress and strain at each domain point, the temperature distribution is only modified here by P_{th}, i.e. $\boldsymbol{\sigma}$, in the infinitesimal strain limit considered in this work (the Lagrangian and Eulerian description are indeed the same in this limit). By contrast, the direct influence of the strain on T, via effective geometry changes, would require finite strain models with dynamically moving mesh.

The volumetric coefficient of thermal expansion[34] α_V is related to the (linear) secant coefficient of thermal expansion α_L through $\alpha_V = 3\alpha_L$ since the thermal strain $\boldsymbol{\epsilon}_{th}$ is $\boldsymbol{\epsilon}_{th} = \alpha_L (T - T_{ref})\boldsymbol{I}$, where T_{ref} is the reference temperature at which there are no thermal strains. Unlike the terms in equation (1), all the physical parameters (K, G, α_L) of equation (2) are assumed to be constant in this work and are provided in table II (K and α_L can be deduced from the EoS, adding a coupling between equations 1 and 2).

Because of its multi-physics nature, our axisymmetric numerical model is developed using the finite element commercial software COMSOL, which is well suited for such modelling. It is important to notice that numerical difficulties are raised by the large disparity of time and space scales involved in our DAC numerical model. To ensure accurate integration in space and time of equations (1)-(2), special care has thus been taken concerning the mesh and the time-stepping (Appendix C).

At first, our model has been benchmarked with a previous publication[28]. However, the pressure-temperature variations of different material properties (see Table II for more details) have been hereby included, which could lead to temperature differences as high as 7000 K at both the center and the boundary of the sample (Fig. 5). To be more specific, Figure 5 shows that the material parameter's P and T variations play a major role. The thermal pressure effect seems less important overall, but nevertheless reaches up to 5 GPa in our model.

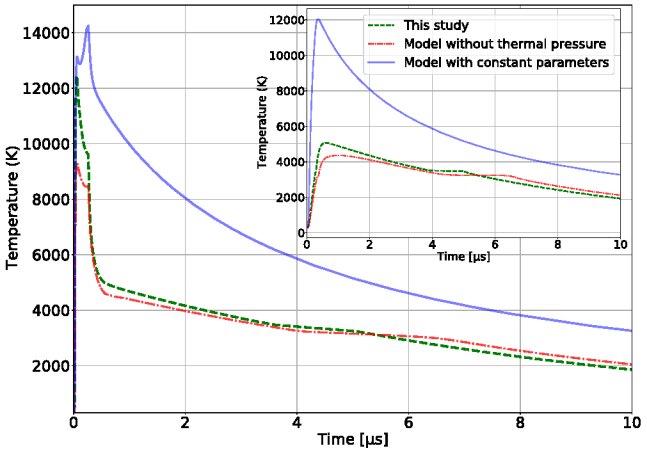

FIG. 5. Time evolution of the sample temperature (on the symmetry axis), at its upper boundary (UBS, main figure) and at its center (MS, inset). Green dashed line: present model. Solid blue line: previously used model[28] (constant material parameters). Dashed dotted red line: present model, disregarding the thermal pressure.

Besides, discarding the thermal pressure in our model leads to a significant 3000 K temperature difference on the maximum temperature reached at the sample boundary (see the maxima in the figure 5). Thus, these effects cannot be neglected when comparing numerical models to experiments.

IV. RESULTS AND DISCUSSION

The present study combines FEM modeling with newly designed MHz XRD in pulsed LH-DAC experiments, which constitutes an innovative scientific approach to study partial melting at high pressure. After the description of the experimental and numerical methodology, the applications to partial melting in the ternary Fe-Si-O system will be described. First, calculated temperature histories are compared to time-resolved XRD data. After, model temperatures will be compared to the solidification temperatures of Fe-Si alloys. This provides a benchmark for our FEM model and validates the extrapolation of model temperatures to times and conditions outside the range measured by SOP.

An example of SOP raw data and Planck fitting used to obtain temperature data can be found in the supplementary material. The peak SOP temperature is poorly resolved due to less signal, rapid variation, possible signal saturation at very high temperatures, as well as eventual KCl optical property variations at highest temperatures[50]. Temperature decay over several microseconds, on the other hand, is well constrained and constitutes the main focus of this study.

As shown in Figure 6, a FEM model including laser heating only is adjusted on the SOP data by finding the proper incoming intensity which minimizes the difference between SOP and model temperature evolution at the upper border of the sample (UBS). Results for the run shown in figure 6 underline the fact that optimal laser energy has the same order of magnitude to experimentally measured energy (around 1 mJ

TABLE II. List of material properties used for our simulation. All parameters mentioned by "var." are varying with the model temperature and pressure outputs. References for those variations are given in the footnotes of this table. When the same value is used for different phases, those are mentioned in parenthesis. If only one value is given this means that the same was used for all phases. X-ray absorption coefficients[28] μ are given for 25 keV and laser absorption coefficients are given for a 1 µm wavelength.

	Fe (hcp/fcc/liq)	KCl (sol/liq)	Diamond	Re
μ_{Laser} (m^{-1})[a]	∞	7×10^{-4}[b]	0.3[c]	0
$\mu_{\text{X-ray}}(\text{m}^{-1})$ (18 keV)	26316[d]	2513[d]	158[d]	0
C_{P} (J.(kg.K)^{-1})	var.[e](hcp,fcc)/900[42]	690.72[f]	630[g]	140[g]
$k_{th}(\text{W.(m.K)}^{-1})$	var.[27]	6.53[f]/0.344[43]	1500[g]	48[g]
$\rho(\text{kg.m}^{-3})$	var.[36]/var.[37]/var.[38]	var.[25]/var.[44]	3520[g]	21020[g]
α_L (K^{-1})	12×10^{-6}	36.5×10^{-6}	0.8×10^{-6}	6×10^{-6}
G (GPa)	78[h](hcp/fcc)/0	6.24[f]/0	529.6[i]	182[h]
K (GPa)	160[j]	17.2[k]	446[l]	312[h]

[a] See supplementary material
[b] Hass et al. 1976[40]
[c] Values for IIa diamonds[41]
[d] https://henke.lbl.gov/optical_constants/atten2.html
[e] Relationship detailed in Appendix C
[f] https://www.crystran.co.uk (see supplementary material for full references)
[g] Meza-Galvez 2020[28]
[h] AZO materials (see supplementary material for reference)
[i] Klein et al. 1993[45]
[j] Rajabpour et al. 2015[46]
[k] Kinoshita et al. 2005[47]
[l] At ambient conditions[48]

acquired at laser output before being split in two parts) as shown in the inset of Figure 6. The inset of figure 6 plots the mean error between SOP temperature data and FEM model temperature at different laser intensities on one heating spot of the FeSiO alloy. The model with lowest mean error is selected and used to plot the corresponding COMSOL temperature curves as a function of time (Fig. 6). Good agreement between the SOP temperature data and model temperatures are found after minimization.

The first appearance of SiO_2 diffraction lines is dominated by few crystallites which oscillate in and out of the bragg diffraction condition. As a result, the observed diffraction intensity varies with time. Additionally, SiO_2 diffraction intensity is weaker than the Fe-Si alloys which crystallize at lower temperatures. Finally, the downstream mirror is slightly shadowing the low diffraction angles on the X-ray detector. For all those reasons, it is complex to identify the first crystallization of SiO_2. However, we have been able to determine the first appearance at 2.2 µs (Fig. 6) on the run presented in Figure 3, which corresponds to a lower temperature limit of 4400 K. Comparing this temperature with the crystallization of pure SiO_2 (5200 K[52]) we can extract the liquidus temperature of the FeSiO ternary system. These results are presented in Figure 7. This liquidus temperature may not be significantly affected by recrystallization kinetics of SiO_2, as shock experiments recently demonstrated the ns timescale for SiO_2 crystallization from melt[53,54].

The main goal of the experiment was to limit chemical migration during laser heating. As a proof of concept, we analyzed the chemical composition of several heating spots after heating. Fig. 8 presents a typical heating spot obtained after a single heating event. The cross section of figure 8 compares the mean relative chemical compositions in weight percent between the pristine sample and heated areas (list of measurements and specific point location provided respectively in Table III and figure 13). This is the main difference with previous measurements performed at longer heating durations (over 1 second)[9], where liquid compositions were found to have an O content around 0.1 wt% for similar pressure. We can discuss the presence of temperature gradients in our probed sample using our model (Fig. 9). Indeed figure 9 highlights differences between UBS, middle of the sample (MS), minimum and maximum temperatures inside the 5 µm radius cylindrical zone sampled by the X-rays as a function of time. During the first 250 ns, there are temperature gradients greater than 10000 K in the probed volume. A first temperature homogenization occurs after 1 µs with around 900 K between minimum and maximum temperature within the X-ray sampled zone (inset Fig. 9). Later, around 7 µs, this temperature gradient is reduced to 70 K, confirming the local temperature homogeneity inside the X-ray sampled zone at that time. Temperature maps and extended time range of temperature difference between minimal and maximal temperature reached within X-ray sampled zone as well as associated pressure maps are available in Appendix C 7. Migration time scales observed in continuous laser heating therefore must occur on longer time scales than a few µs, as we do not observe any qualitative difference in composition between the molten area and the starting material.

The absence of relative concentration difference demonstrates that the use of a short-time scale heating pulse reduces chemical migration compared to longer timescale heat-

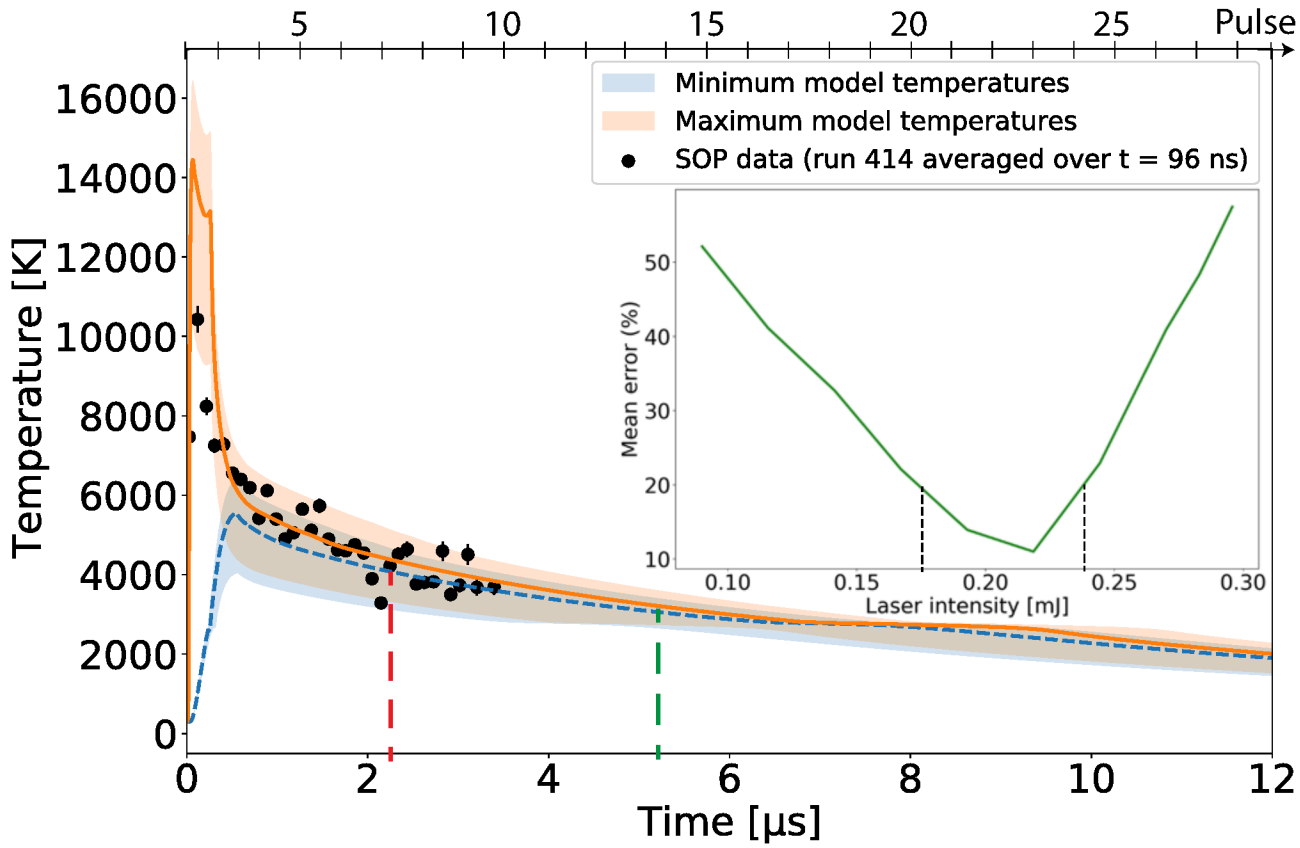

FIG. 6. FEM model temperatures vs time minimizing mean error to experimental SOP temperatures over a single run[a] consisting of a 40-pulse X-ray pulse train shot through a FeSiO sample ($P_{ref} = 61.9$ GPa). Continuous orange line: model temperatures at UBS on axis of symmetry. Black dots are SOP values averaged over 96 ns (model values compared to SOP were averaged over the same duration taking +/- 48 ns around SOP times). Dashed blue curve plots minimum temperature in sample inside the X-ray sampled zone (FWHM = 5 µm). Vertical red and green dashed lines respectively show the times where SiO_2 (2.2 µs) and Fe-7 %Si-fcc[51] (5.198 µs) are unambiguously observed by XRD. Inset: Mean error between model UBS and SOP temperatures for several laser intensities. The wave-plate rotation angle was 20°upstream and downstream (relationship between measured laser intensity and wave-plate rotation angle can be found in supplementary material). Vertical black dotted lines bracket best models obtained within 20% mean error (which were chosen as corresponding error bar).

[a] Exp 2605 run # 414

ing where chemical migration is observed on the FeSiO alloy[9] with SiO_2 accumulating at the external boundaries of the heated spot. Moreover, the post-experiment XRD mapping is an additional proof of the absence of strong chemical migration, with the presence of intense SiO_2 XRD signal over the entire hotspot (see supplementary material).

Additionally the model minimum temperature curve (figure 6) can be compared with the FeSi-fcc phase nucleation point. The time of crystallization is obtained by the time of appearance of the FeSi-fcc on the diffraction spectra (Fig. 3). As a first approximation the pressure is considered to be the initial one measured within the KCl volume (around 62 GPa for the example in Fig. 6). Agreement can be observed between model extrapolated SOP data and expected crystallization temperature[51] ranging between 2000 and 3000 K around 60 GPa (blue dotted curve vs green squares in figure 6).

Crystallization times for Fe-Si alloys are bracketed between fully molten and first solid crystal appearance (Figs. 6 and 7). Note that we do not take into account here any crystallization kinetics for FeSi alloys which is more pertinent at the 100 ps time scale[56]. Crystallization pressures and temperatures were evaluated by combining model output temperature (minimum temperature within sample inside a radius of 5 µm) and pressures obtained with two different methods: (i) pressure obtained with $P(V,T)$ EoS[25] using calculated mean temperature in KCl with the method described in Campbell et al. 2009[16] and volume obtained by XRD (in the case of KCl peak broadening due to temperature gradient, the mean peak position was selected assuming it to be the mean PTM lattice volume), or (ii) mean total pressure ($P_{ref} + P_{th}$) in sample (over r=5 µm) from model output. In the ternary Fe-Si-O phase diagram, the crystallization of the Fe-Si alloy is expected not to incorporate any oxygen[9] and therefore fall close to the Fe-Si binary system (Figs. 2 and 7). Following the demixing line, the crystallizing Fe-Si alloy contains 7 wt%Si. This is shown on the binary cross section presented in figure 7. Figure 10 melting points could thus be compared with Fe-7wt%Si[51] and Fe-9wt%Si[55] melting curves. Points obtained by the two methods

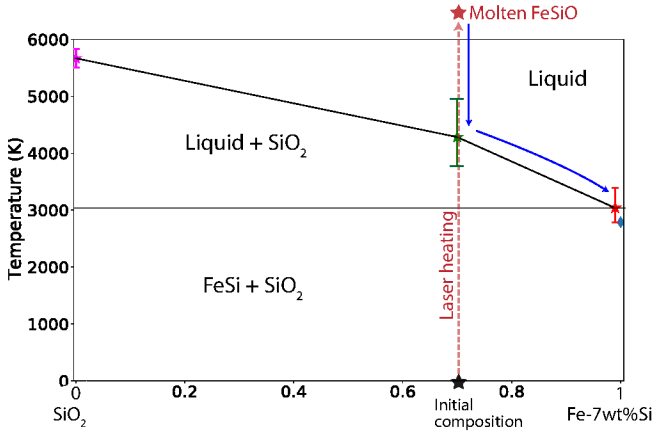

FIG. 7. Binary phase diagram reconstructed between SiO_2 and Fe-7wt%Si (see Fig.2). The different points were obtained from XRD phase appearance points (Fig. 3) from a single run (# 414) and melting temperature of pure SiO_2[52] (upper left purple star). Initial alloy's composition is represented by the black star at the bottom. Phase appearance temperatures of SiO_2 (green star in the middle) and, subsequently FeSi (red star on the right) were obtained using the best SOP vs model temperature fit at the corresponding timings. We chose the minimum sample temperature from the model in the X-ray sampled zone assuming it to be the location of the first crystal appearance. The blue diamond represents the melting temperature of Fe-7wt%Si from literature[51] at the model mean pressure (around 65 GPa) inside X-ray probed area. Arrows indicate the pathway taken by the sample upon heating (orange dashed arrow) and cooling (blue continuous arrow), highlighting how Fe-Si-O liquidus is caught during the experiments. The sample composition crossing the liquidus is assumed to be the same as the initial one.

are consistent with existing literature within uncertainties, as shown in figure 10. The absence of thermal stress feedback in the PTM temperature in the first case explains observed pressure differences with the second case, where thermal pressure is modeled inside the sample.

The estimated pressure, temperature couples are then compared with the Fe-Si alloy melting curves (Fig. 10) taken from existing literature[51,55]. Despite the different thermal pressures depending on the assumption, we can observe an overall agreement between our measurements and the existing literature. This allows to conclude that the temperature extrapolated using our FEM model are relatively well benchmarked with previously established Fe-Si melting curves.

V. CONCLUSION

This study validates a new approach where crystallization sequences upon cooling from a homogeneous liquid state with limited chemical migration due to heating are reproduced. Diffraction data collected during several heating cycles (Fig. 3) combined with chemical analysis (Fig. 8) confirmed the reduced amount of chemical migration induced by short laser heating pulses. This enabled, in some cases, to observe the successive phase appearance of SiO_2 and FeSi-fcc phase. The detection of SiO_2 peaks at low diffraction angles remains difficult. This is partly due to technical aspects such as the limited coverage of the AGIPD, which only collects partial diffraction rings. However, we can still present here a measurement of liquidus temperature with the SiO_2 recrystallization from the liquid (Fig 7).

This opens up a new pathway for future "chemical-migration limited" experiments, giving access to phase diagrams and melting curves of previously never explored phases and alloys. In that frame numerical simulations are required to solve for temperature gradients, particularly strong during the first microseconds of the heating phase, as well as to provide accurate global temperature evolution and constrain the amount of thermal pressure. Model and experimental data are complementary for X-ray diffraction data interpretation. Models can constrain the contribution of the different phenomena leading to the chemical migration, knowledge which, in turn, could lead to adapted experimental designs. For higher accuracy in experiment reproduction, future models should include real-time deformations, take into account reported non-isotropy[49], liquid-liquid interface movements (PTM/sample) as well as phase separation and grain growth.

VI. SUPPLEMENTARY MATERIAL

Supplementary material provides (i) explanation about how X-ray heating could be excluded from our FEM model, (ii) 2D XRD maps with heating spot localization, (iii) details about some parameters choices made in the model, (iv) details about SOP measurements, (v) relationship between power and wave-plate rotation angle, (vi) explanations about boundary conditions in our model, (vii) melting curves, and (viii) the exact model geometry of our numerical model.

The data that support the findings of this study are available from the corresponding author upon reasonable request.

Data recorded for the experiment at the European XFEL are available at "10.22003/XFEL.EU-DATA-002605-00."

ACKNOWLEDGMENTS

The authors are indebted to the HIBEF user consortium for the provision of instrumentation and staff that enabled this experiment. We acknowledge European XFEL in Schenefeld, Germany, for provision of X-ray free-electron laser beamtime at Scientific Instrument HED (High Energy Density Science) and would like to thank the staff for their assistance. This research was supported through the European Union's Horizon 2020 research and innovation program (ERC grant 864877 & 101002868, and DC was partially supported by the ERC grant 847433) as well as UKRI STFC grant ST/V000527/1. This project was also financed by IDEX Université Grenoble Alpes. In addition, NJ has been supported by a grant from Labex OSUG@2020 (Investissements d'avenir – ANR10 LABX56). KB would like to acknowledge funding by Deutsche Forschungsgemeinschaft via Ap 262/2-2 within the DFG-FOR2440 HP4. YL thanks the support from the

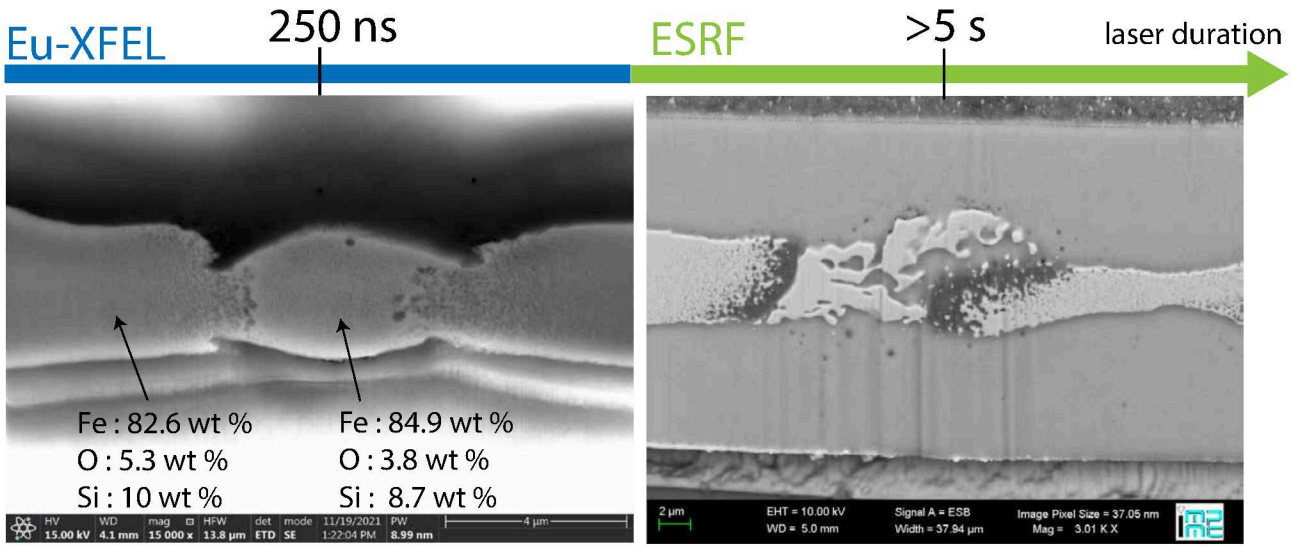

FIG. 8. SEM cross sections comparing FeSiO alloy samples with same composition heated at 250 ns (left) and >5 s (right), with KCl pressure medium. Right image: heated region (center) is homogeneous, with possible grain growth and/or chemical migration at the heating spot edges. Major element distribution in the heated and unheated portions of the sample are given (full chemical analysis in Appendix B). This illustrating run is not the one compared with our FEM model [where δ_3 (Table I) is e.g. different]. No chemical measurement was done on the right sample but its composition is the same as the one used in Hirose et al. 2017[9]. It is therefore expected to show the same chemical distribution upon heating (i.e. darker parts at heating spot edges are SiO_2 enriched zones and middle part Fe enriched).

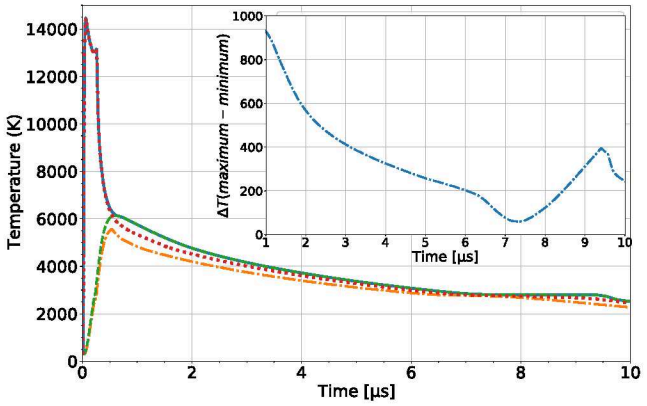

FIG. 9. FEM model temperatures (K) as a function of time (µs) at different points of the geometry. The red dotted line represents the temperature at the upper border of the sample (UBS) whereas the green dashed line stands for the temperature in the middle of the sample (MS), both lying on the axis of symmetry. The two other temperature curves show minimum (orange dotted-dashed line) and maximum (blue continuous line) temperatures inside of the X-ray sampled zone (cylinder of 5 µm radius). Inset: Difference between the minimum and maximum temperature reached inside the X-ray sampled zone. It can be observed that a local temperature gradient minimum is reached around 7.25 µs where the maximum temperature difference inside the X-ray sampled zone is only 70 K

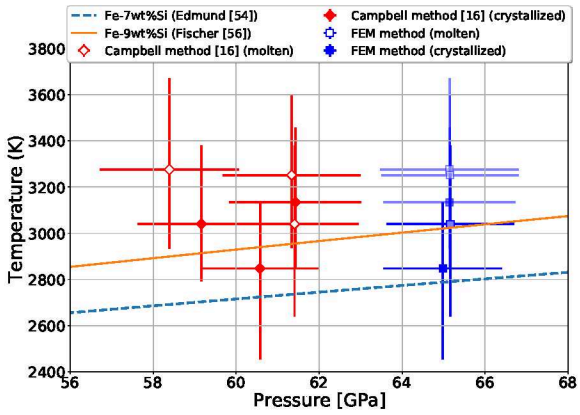

FIG. 10. FeSi-fcc melting points at pressures inferred from two methods: 1) Red diamonds represent the melting points with pressures $P(V,T)$ calculated using KCl EoS[25] with T the mean KCl temperature calculated via method described by Campbell et al. 2009[16]). 2) Blue squares are at mean model's pressure ($P_{ref}+P_{th}$) in sample in X-ray sampled zone. In both cases, the EoS input lattice volume V_{diff} was obtained from KCl mean peak position and melting temperature was assumed to be the minimum model temperature within X-ray sampled zone at the respective time. Dotted blue line: Fe with 7 wt%Si[51] melting curve, continuous orange line: Fe with 9 wt%Si[55] melting curve. Error bars are obtained from the two second best SOP fitting models.

Leader Researcher program (No. NRF-2018R1A3B1052042) of the Korean Ministry of Science and ICT (MSIT). A.F.G acknowledges support of National Science Foundation grant No. DMR-2200670. We acknowledge as well funding from the Programme National de Planetologie (PNP) of CNRS/INSU, co-funded by CNES. Thank you to James Moore for the help on the FIB.

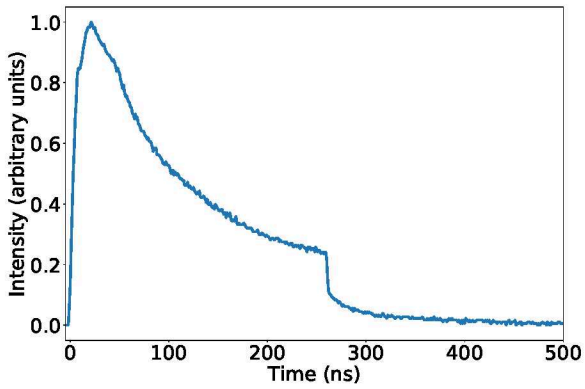

FIG. 11. Time evolution of the fiber laser intensity I_{meas}, acquired with an oscilloscope at the EuXFEL, and used in our experiments. The intensity has been normalized here to have a unit maximum intensity.

Appendix A: Laser and X-ray beams temporal evolution

To ensure a high model fidelity with the real experimental conditions, the time dependency of the fiber laser intensity was included. This intensity variation was measured by an oscilloscope and is plotted in Figure 11 with a 994 values file directly implemented in the model.

The X-ray pulse train series used in the model was implemented by reproducing a series of Gaussian pulses (figure 12). The temporal width of each pulse (P_{dur}) is the same, linked to the standard deviation σ_t=30 fs by $P_{dur} = \sigma_t 2\sqrt{2\ln 2}$. In the following a pulse is a truncated Gaussian curve within a range of $[-4\sigma_t, 4\sigma_t]$. Duration between pulses is kept constant and is related to the frequency by $P_X = 1/f_X$, with $f_X = 2.257$ MHz such that an X-ray pulse hits the sample every 443 ns. Finally, we decided not to start the first pulse of the series at exactly zero due to numerical issues when dealing with extremely small numbers (of the order of the machine precision). Therefore, the first pulse is chosen to start at $128\sigma_t$ which corresponds to a reasonably "numerically detectable" starting duration for the COMSOL software. We generated value files including 50 values per pulse, each pulse in the around the maximum peak value and zeros elsewhere. This file is then imported into our COMSOL model. It is hereby important to notify that the software reduces the precision.

To reproduce the incoming energy due to the X-ray pulse train, we generate a series of Gaussian pulses (40 in that specific case) at a frequency of 2.257 MHz. Each pulse is assumed to have the exact same duration with the standard deviation given by $\sigma_t = S_{Diam}/[2\sqrt{2\ln 2}]$). Pulse peak intensity is known to vary within a pulse train and was therefore normalized to 1 as the maximum of the highest intensity. In order to ensure a realistic agreement between the model and experimental results, we impacted the X-ray intensity variations measured during our runs onto this bunch of pulses (supplementary material). Each pulse of the train was weighted by the measured intensity. Details about the exact pulse series

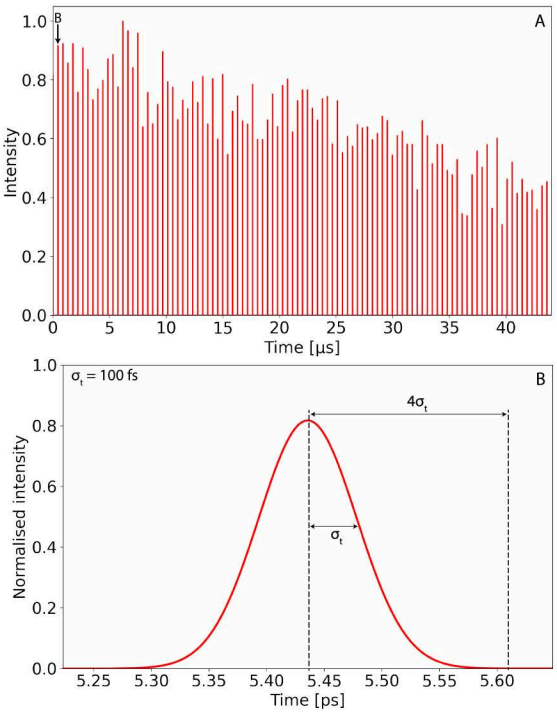

FIG. 12. A. Pulse series example for a run showing intensity variation inside a pulse train (in a.u.) as a function of time (in µs). B. Focus on single X-ray pulse intensity as a function of time. Intensity is normalized to 1 corresponding to the maximum intensity reached in the pulsed train.

generation procedure used for the model are given in figure 12. Figure 12 (A) plots the entire pulse train normalized to 1 as the maximum intensity reached in the entire train. Fig. 12 (B) highlights the shape of the first pulse.

Appendix B: FIB cutting chemical analysis

An FEI HELIOS G4 UC FIB/SEM was used to access the heating spots and check for apparent chemical migration phenomena. The shot observation combined with chemical analysis with an EDS detector demonstrated that no apparent chemical migration occurred for short laser heating. In addition, supplementary *post mortem* analysis was achieved with FIB cutting. Along FIB cutting, chemical analysis was performed with a Helios G4 UC FIB/SEM. Table III lists the measured concentrations in each element in weight percent (wt%) and figure 13 refers to the localization of each measurement (8 in total). Depletion of up to 3.15 wt% of O and 3.56 wt% of Si and enrichment up to 6.17 wt% iron were observed in the heating spot compared to the pristine sample. However this is the highest observed difference and certain spot show differences as low as 0.73 wt% of O (pt2 vs pt8), 0.39 wt% of Si (pt2 vs pt 6) and 0.59 wt% Fe (pt2 vs pt5). We estimate the error bar on the chemical measurements to be relatively larger than conventional microprobe measurements, as we were only

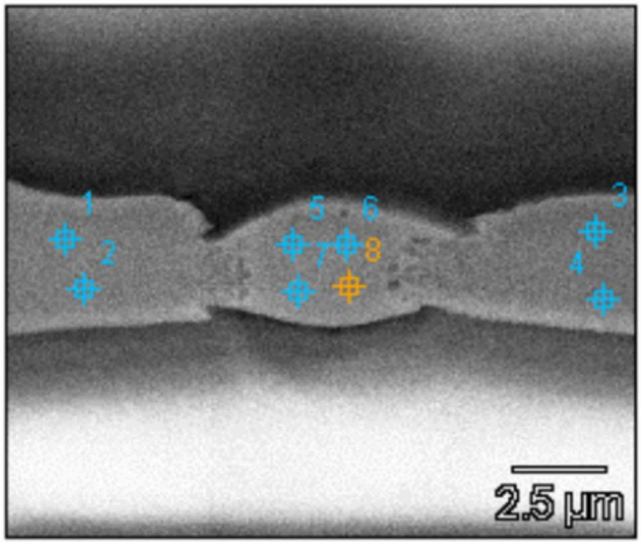

FIG. 13. Localization of chemical EDS analysis. For points, refer to Table III

Meas. point/ chem. species	O	Si	Cl	K	Fe
Point 1	5.63	10.61	1.02	1.11	81.63
Point 2	5.04	9.4	0.93	1.07	83.57
Point 3	6.23	11.53	0.99	1.05	80.2
Point 4	5.53	10.11	1.02	0.94	82.4
Point 5	4.21	8.98	1.47	1.18	84.16
Point 6	3.71	9.01	1.7	1.17	84.41
Point 7	3.08	7.97	1.54	1.05	86.37
Point 8	4.31	8.76	1.32	1.07	84.54

TABLE III. Concentration measurements from FIB (in wt%)

able to perform EDS measurements in a tilted geometry during FIB cut. However, the present measurements are used to characterize the chemical migration, i.e. the relative composition between unheated starting material and center of the laser heated hotspot.

Appendix C: Details on our numerical model

Modeling the DAC geometry with a simple Cartesian 2D model is possible, but it would discard our DAC symmetry of revolution. With nearly the same numerical cost, our DAC is better modeled by an axisymmetric model[28], assuming only radial or axial variations and using a 2D mesh (figure 4). Such a model represents accurately the real DAC provided that the laser-heating is well centered on the axis of symmetry, and discarding possible three-dimensional effects (which could e.g. be due to liquid flows[13]).

1. Pressure induced thickness variation

Regarding the thicknesses mentioned in Table I, the second value corresponds to the theoretical thickness obtained after compression. In the model, We start from a thickness measured at the heating spot location of the sample FIB cross section. This is an approximation used to take plastic deformation into account. The thickness variation related to sample's elastic deformation with pressure in DAC experiments depends on the material and is therefore related to the EoS (ε-Iron[36], liquid iron[38], B2-KCl[25]).

In order to have directly an expression for the volume, we solve the EoS to obtain a multivariate polynomial under the $V(P,T)$ form which is then used for thickness calculations. We calculated the volume of the sample V_S considering the case of a perfect cylinder

$$V_S = \pi R_3^2 \delta_3 \tag{C1}$$

where R_3 is the sample radius, and δ_3 the sample thickness before compression. We consider the simplified case where deformations in the radial direction are neglectable upon first compression due to the gasket resistance. Thus, the sample is only considered to deform in the axial direction (meaning in its thickness). From there on we calculate the initial number of lattice elements N_e in the DAC at ambient pressure

$$N_e = V/V_0, \tag{C2}$$

where V_0 is the sample volume at ambient pressure and temperature which can be found using material properties available in the literature. We assume that the number of lattices remains constant in the sample during compression. The lattice volume is then calculated at the experimental pressure of the DAC using the multivariate polynomial providing $V(P_{ref})$. Finally, we calculate the thickness by rewriting (C1) and including the initial number of lattice elements and their new volume at the desired pressure

$$\delta_3(P_{ref}) = \frac{N_e V(P_{ref})}{\pi R_3^2} \tag{C3}$$

with R_3 being the sample radius. The thickness of the sample as well as that of the PTM are calculated this way as a function of the initial pressure in the DAC. The thickness is then considered being constant during the simulation.

2. Thermal heating due to radiation absorption

In the DAC, the temperature rise is generated by the material absorption of the laser and X-ray beams emitted along the z-axis. In the following, we first consider the intensity of a single beam, incident on the diamond surface; the total intensity in our numerical model is then simply the linear superposition of the laser and X-ray radiation beam intensities.

In each material, the absorption of this single radiation beam is assumed to be governed by the Beer-Lambert law[28], and the absorption occurs on a typical length scale that depends on the radiation frequency and on the material's opacity. When this length scale is very small compared to the material layer thickness, i.e. for opaque materials, this volume absorption can be approximated by a boundary heat source, avoiding

the fine mesh that would be required otherwise (see details in Appendix C 3). In such opaque materials, the radiation intensity is zero below the material's surface, and the volume heat source due to radiation absorption is discarded ($Q = 0$). In the opposite case, the volume absorption in the semi-transparent material layer (k) has to be considered. Considering the radiation intensity I due to the single beam along the unit vector $\hat{\boldsymbol{I}}$, the Beer-Lambert law reads

$$\nabla I = -\mu_k I \hat{\boldsymbol{I}}, \tag{C4}$$

which integrates into (along $\hat{\boldsymbol{I}}$, i.e. along the z axis here)

$$I = I_k^{in} \mathrm{e}^{-\mu_k H_k} \tag{C5}$$

for a constant (Napierian) attenuation coefficient μ_k, which depends naturally on the radiation beam frequency content. Here, $H_k = \pm(z - z_k)$ is the penetration depth in the material (k), the sign depending on the radiation direction and z_k being the z-position of the surface layer that the radiation is incident on. In this material (k), the volume heat source Q_k is then simply given by $Q_k = \mu_k I$.

In principle, μ_k also depends on temperature and pressure, and thus on space, which requires the integration of the partial differential equation (C4). These dependencies being however not well known in our case, constant values have been used for μ_k in our model (Table II). The numerical cost associated with the integration of equation (C4) has then been avoided by using directly the analytical solution (C5) in the model. Table IV provides the various analytical expressions used in the model to reproduce the incoming laser and X-ray intensities and their interaction with the material through absorption (required to calculate Q_k).

Since the total intensity I_k^{tot} incident on the material layer (k) boundary can be partially reflected, the actual incoming intensity I_k^{in} in equation (C5) is $I_k^{in} = (1 - \mathscr{R}_k) I_k^{tot}$, with the material reflection coefficient $\mathscr{R}_k$. Since $\mathscr{R}_k$ is insufficiently known and depends on many parameters like the radiation frequency, the surface roughness or the temperature, all the reflection coefficients are set to $\mathscr{R}_k = 0$ in our model.

Before entering any material or any reflection, the total intensity I_0^{tot} of the radiation incident on the diamond is modeled with a Gaussian spatial distribution such that

$$I_0^{tot} = I_m I_t(t) \exp\left(-\frac{r^2}{2\sigma_r^2}\right), \tag{C6}$$

where $\sigma_r = S_{Diam}/[2\sqrt{2\ln 2}]$ is a Gaussian radius parameter related to the radiation FWHM spot diameter S_{Diam}, and with r the cylindrical radius coordinate (distance from the model symmetry axis). Since the absolute value of the maximum intensity I_m is generally not known for the experiments (both for the laser and the X-ray beam), it is here a model adjustable parameter that is fixed to obtain good agreement between the experimental and the numerical results. By contrast, the temporal evolution $I_t(t)$ imposed in the model is obtained from measurements or modelling of the pulses (see also Appendix A). Integrating equation (C6) in space and time provides the pulse energy E_p as[28]

$$E_p = 2\pi\sigma_r^2 I_m \mathscr{E} \tag{C7}$$

where $\mathscr{E} = \int_t I_t(t)\mathrm{d}t$.

3. Boundary conditions and initial state

To integrate equations (1)-(2), boundary conditions are needed at the external diamond and gasket boundaries.

Heat loss through convection and radiation should usually be considered but as the DAC is placed in vacuum, only radiation plays a role. Yet regarding the possible need of including both ways of heat transfer for future models, more details upon heat transfer are given in supplementary material. For the temperature T, two conditions have been used here. Either a constant external temperature T_{ext} has been imposed at the external boundaries, or heat loss through radiation is considered following in our case a $q_s = \sigma_s(T^4 - T_{ext}^4)$ law with the Stefan-Boltzmann constant $\sigma_s = 5.67 \cdot 10^{-8}$ W.m^{-2}.K^{-4}. Here $T_{ext} = 300$ K is used, and both conditions lead actually to the same results. Indeed, external boundaries are very far from the maximum thermal heating, and the effect of the boundary condition choice can thus be expected to be negligible.

Boundary conditions are also required for the elastic part, and the zero displacement constraint $\boldsymbol{u} = \boldsymbol{0}$ has been imposed at all external boundaries. Note that the thermal pressure P_{th} would naturally be zero if all external boundaries can move freely, and displacement constraints are thus required, at least at certain boundaries, to generate a thermal pressure (preliminary tests have been performed by setting $\boldsymbol{u} = \boldsymbol{0}$ for the diamonds or the gasket only).

In opaque materials, like the metallic sample considered in our experiments, the attenuation coefficient μ is very large and the radiation induced thermal heating occurs then on the very small typical length scale μ^{-1}. This would require a very fine mesh to reproduce the intensity variations given by the Beer-Lambert (volume) absorption equation (C5). To avoid the associated numerical cost, one can rather replace this volume absorption by a boundary heat source, assuming that all the (non-reflected) radiation energy flux I_k^{in} is converted into surface heat at the material surface. Such a surface approximation is fully relevant when μ^{-1} is small compared to the material thickness (e.g. $\mu^{-1} \ll \delta_3$ here). At these boundaries, the normal heat flux is thus imposed to be I_k^{in}. This approach has been benchmarked by checking that the results obtained this way are the same than those obtained with a Beer-Lambert volume absorption model (integrated on a fine mesh). In the simulations shown in this work, such a boundary heat source has only been used at the sample surface, the least being highly absorbing (i.e. opaque) at laser wavelength. Note that this boundary heat source approach reduces the numerical cost while keeping realistic physical behaviour. Rather thin meshes are yet required and a numerical convergence study has to be carefully performed to ensure the numerical accuracy of the results.

Finally, the transient response of our numerical DAC, obtained by time-stepping equations (1)-(2), heavily depends on the chosen initial state. Here, the model integration starts with a constant temperature $T(t = 0) = T_{ext} = 300$ K and with the zero initial displacement $\boldsymbol{u}(t = 0) = \boldsymbol{0}$ initial state (no initial

Medium	X-ray volume heat source	laser volume heat source
1	$I_{X_0}^{tot}\mu_{X_1}\exp(\mu_{X_1}(z-(\delta_1+\delta_2+0.5\delta_3)))$	$I_{L_0}^{tot}\alpha_1\exp(\mu_{L_1}(z-(\delta_1+\delta_2+0.5\delta_3)))$
2	$I_{X_1}^{tot}\mu_{X_2}\exp(\mu_{X_2}(z-(\delta_2+0.5\delta_3)))\exp(-\mu_{X_1}\delta_1)$	$I_{L_1}^{tot}\mu_{L_2}\exp(\mu_{L_2}(z-(\delta_2+0.5\delta_3)))\exp(-\mu_{L_1}\delta_1)$
3	$I_{X_2}^{tot}\mu_{X_3}\mathrm{e}^{-\mu_{X_2}(z+\delta_2+0.5\delta_3)}\exp(-\mu_{X_1}\delta_1)\exp(-\mu_{X_2}\delta_2)$	$\varnothing$
4	$I_{X_3}^{tot}\mu_{X_2}\exp(-\mu_{X_2}(z+\delta_2+0.5\delta_3))\varpi$	$I_{L_1}^{tot}\mu_{L_2}\exp(\mu_{L_2}(z-(\delta_2+0.5\delta_3)))\exp(-\mu_{L_1}\delta_1)$
5	$I_{X_4}^{tot}\mu_{X_1}\exp(-\mu_{X_1}(z+(\delta_1+\delta_2+0.5\delta_3)))\exp(-\mu_{X_4}\delta_4)\varpi$	$I_{L_0}^{tot}\mu_{L_1}\exp(\mu_{L_1}(z-(\delta_1+\delta_2+0.5\delta_3)))$

TABLE IV. Beer-Lambert solutions for $Q_k=\mu_k I$, as used in COMSOL, noting $\varpi=\exp(-\mu_{X_1}\delta_1)\exp(-\mu_{X_2}\delta_2)\exp(-\mu_{X_3}\delta_3)$. Absorption coefficients were adapted depending on the heating source wavelength (X-ray or laser). Formula for the sample only applies in the case of X-rays, wavelength at which Fe is semi-transparent on the contrary to fiber laser wavelength where all energy $I_{L_2}^{tot}$ is considered to be deposited at the surface on both sides of the sample. Numbered labels in Table IV are listed as (1) upstream diamond of thickness δ_1, (2) upstream PTM of thickness δ_2, (3) sample of thickness δ_3, (4) downstream PTM of thickness δ_2, (5) downstream diamond of thickness δ_1. For the laser, I_0^{tot} and I_5^{tot} have the same value due to two sided heating. Same for I_4^{tot} and I_2^{tot}. μ_{X_i} and μ_{L_i} stand respectively for the X-ray and laser absorption coefficients in the ith medium. The same for the intensities $I_{X_i}^{tot}$ and $I_{L_i}^{tot}$.

condition is required for the time derivative of $\boldsymbol{u}$, i.e. for the initial velocity, since our approach is quasi-static).

4. Heat capacity of the hcp-iron

Lots of parameters rely on these EoS due to their dependency to volume, temperature and/or pressure (sample thickness, thermal conductivity, heat capacity).

In addition to material property variations with temperature and pressure along a given phase, phase variations occur upon laser, X-ray heating and compression. Those phase changes affect the material properties and were implemented by referring to the phase diagrams available in the literature. Melting curves and phase change zones were taken into account in the model by using them as conditions for parameter changes. This model uses existing melting curves for iron alloys[57,58,59] and KCl[60] (provided in supplementary material).

The specific phase change between hcp and fcc high pressure phase of iron was included in the model using a second order polynomial[3]. Phase changes are mostly related to material property modifications. Therefore we used the phase change temperature as a condition for switching EoS[36,37]. As phase changes generally go along with a release or absorption of latent heat we included as well the Apparent Heat Capacity Method (AHCM). Heat capacity variations as a function of temperature and pressure can be inferred from the formula given by Komabayashi et al. 2014[61]

$$G=G_0+\int_{10^5 Pa}^{P}V_T\mathrm{d}P \tag{C8}$$

where G is the Gibbs free energy, G_0 the Gibbs free energy at $P=10^5$ Pa and given T expressed by

$$G_0=a_0+a_1T+a_2T\ln T+a_3T^2+a_4T^{-1}+a_5T^{0.5} \tag{C9}$$

with $a_0=12460.621, a_1=386.99162, a_2=-52.2754, a_3=0.000177578, a_4=-395355.43, a_5=-2476.28$ and V_T the molar volume of the corresponding phase at given T where the EoS obtained multivariate polynomial is used.

In order to obtain C_P, we use[62] :

$$S=-\left(\frac{dG}{dT}\right)_P \quad , \quad \left(\frac{dS}{dT}\right)_P=\frac{C_P}{T} \tag{C10}$$

that can be combined, leading to

$$C_P=-\left(\frac{d^2G}{d^2T}\right)_P T \tag{C11}$$

5. Phase change effects

Available as a built-in feature in COMSOL, the Apparent Heat Capacity Method (AHCM) allows to model phase change effects by integrating a single heat transfer equation with effective material properties (the phase change latent heat being included by considering an apparent heat capacity). In this approach, the phase change is assumed to occur over a temperature range ΔT, governed by a smooth phase transition function. The sharpness of the transition is thus controlled by ΔT, which should be wide enough to be accurately captured by the numerical scheme (without any numerical convergence issue). In our case, numerical tests show that $\Delta T=50$ K provides a sharp enough phase change at a reasonable numerical cost. Naturally, this apparent heat transfer equation also use an effective thermal conductivity and density (more details on this built-in AHCM can be found in the COMSOL documentation).

Following this smooth phase change approach, the shear modulus transition from solid to liquid has also been modeled with an shear modulus G given by

$$G=G_l+\frac{G_s-G_l}{2}\left[1-\frac{2}{\pi}\arctan\left(\frac{T-T_m}{W}\right)\right] \tag{C12}$$

with the liquid shear modulus $G_l=0$, the solid shear modulus G_s, the melting temperature T_m of the given phase and where the sharpness of the transition is controlled by the typical temperature range W (fixed to $W=50$ K in our case).

6. Space and time numerical discretization

We used a mesh combined of fine boundary layer type rectangular elements at the sample boundaries, and triangular mesh in the remaining domain. Both element types were

set to be increasingly fine towards the sample boundaries. Diamonds and gasket are on the contrary only meshed by coarse elements regarding the low endured gradients. Using first order Lagrange elements for temperature and elastic displacement, the total number of degrees of freedom is of the 10^4 order for our numerical model.

Equations are time stepped with the built-in time-stepping scheme based on backward differentiation formula[63], and, at each time step the system is solved with the sparse direct linear solver PARDISO[64]. Note that our model involves a large disparity of time scales (down to the fs during a pulse, ns between pulses, µs for the whole simulation duration), which can lead to numerical issues. To ensure that our model takes correctly into account each X-ray pulse over the whole simulation time, the model relies on the 'events' module of COMSOL, which allow specifying the occurrence of a repeated event (forcing a small enough time step at each event).

7. Temperature gradients in sample revealed by modelling.

Differences between minimum and maximum temperatures reached within the X-ray sampled zone can easily be followed with our model as demonstrated in Figure 14. Top three figures show model temperature maps at t=0.4 µs, 1 µs, 7.04 µs (respectively from left to right) where the heat distribution evolution transmitted by the laser pulse is highlighted. Temperature gradients around the first 0.25 µs are as high as 14000 K before a relative temperature homogenization below 1000 K after half µs. Finally as described before, a high temperature homogeneity (below 100 K) is reached little after 7 µs. Bottom graphs of figure 14 are split in two parts for visual convenience, supplementary proof of huge temperature gradients endured by the sample. This underlines that despite important gradients of thousand of kelvin, their short duration lead to almost no chemical migration, calling attention to the fact that chemical migration related phenomena occur at longer time scales than 0.5 µs.

[1] L. T. Elkins-Tanton, "Magma oceans in the inner solar system," Annual Review of Earth and Planetary Sciences **40**, 113–139 (2012).

[2] L. Schaefer and L. T. Elkins-Tanton, "Magma oceans as a critical stage in the tectonic development of rocky planets," Philosophical Transactions of the Royal Society A: Mathematical, Physical and Engineering Sciences **376**, 20180109 (2018), https://royalsocietypublishing.org/doi/pdf/10.1098/rsta.2018.0109.

[3] G. Morard, S. Boccato, A. D. Rosa, S. Anzellini, F. Miozzi, L. Henry, G. Garbarino, M. Mezouar, M. Harmand, F. Guyot, *et al.*, "Solving controversies on the iron phase diagram under high pressure," Geophysical Research Letters **45**, 11–074 (2018).

[4] S. Anzellini, A. Dewaele, M. Mezouar, P. Loubeyre, and G. Morard, "Melting of iron at earth's inner core boundary based on fast x-ray diffraction," Science (New York, N.Y.) **340**, 464–6 (2013).

[5] R. Sinmyo, K. Hirose, and Y. Ohishi, "Melting curve of iron to 290 gpa determined in a resistance-heated diamond-anvil cell," Earth and Planetary Science Letters **510**, 45–52 (2019).

[6] V. Prakapenka, G. Shen, and L. Dubrovinsky, "Carbon transport in diamond anvil cell," High Temperatures-high Pressures - HIGH TEMP-HIGH PRESS **35-6**, 237–249 (2010).

[7] R. Sinmyo and K. Hirose, "The soret diffusion in laser-heated diamond-anvil cell," Physics of the Earth and Planetary Interiors **180**, 172–178 (2010).

[8] R. Sinmyo, K. Hirose, D. Nishio-Hamane, Y. Seto, K. Fujino, N. Sata, and Y. Ohishi, "Partitioning of iron between perovskite/postperovskite and ferropericlase in the lower mantle," Journal of Geophysical Research: Solid Earth **113** (2008).

[9] K. Hirose, G. Morard, R. Sinmyo, K. Umemoto, J. Hernlund, G. Helffrich, and S. Labrosse, "Crystallization of silicon dioxide and compositional evolution of the earth's core." Nature **543**, 99–102 (2017).

[10] M. A. Baron, G. Fiquet, G. Morard, F. Miozzi, I. Esteve, B. Doisneau, A. S. Pakhomova, Y. Ricard, and F. Guyot, "Melting of basaltic lithologies in the earth's lower mantle," Physics of the Earth and Planetary Interiors **333**, 106938 (2022).

[11] C. Lesher and D. Walker, "Cumulate maturation and melt migration in a temperature gradient," Journal of Geophysical Research: Solid Earth **93**, 10295–10311 (1988).

[12] D. Stevenson, "On the role of surface tension in the migration of melts and fluids," Geophysical Research Letters **13**, 1149–1152 (1986).

[13] N. Gomez-Perez, J. Rodriguez, and R. McWilliams, "Finite element modeling of melting and fluid flow in the laser-heated diamond-anvil cell," Journal of Applied Physics **121** (2017).

[14] H. P. Liermann, Z. Konôpková, K. Appel, C. Prescher, A. Schropp, V. Cerantola, R. J. Husband, J. D. McHardy, M. I. McMahon, R. S. McWilliams, C. M. Pépin, J. Mainberger, M. Roeper, A. Berghäuser, H. Damker, P. Talkovski, M. Foese, N. Kujala, O. B. Ball, M. A. Baron, R. Briggs, M. Bykov, E. Bykova, J. Chantel, A. L. Coleman, H. Cynn, D. Dattelbaum, L. E. Dresselhaus-Marais, J. H. Eggert, L. Ehm, W. J. Evans, G. Fiquet, M. Frost, K. Glazyrin, A. F. Goncharov, H. Hwang, Z. Jenei, J.-Y. Kim, F. Langenhorst, Y. Lee, M. Makita, H. Marquardt, E. E. McBride, S. Merkel, G. Morard, E. F. O'Bannon, III, C. Otzen, E. J. Pace, A. Pelka, J. S. Pigott, V. B. Prakapenka, R. Redmer, C. Sanchez-Valle, M. Schoelmerich, S. Speziale, G. Spiekermann, B. T. Sturtevant, S. Toleikis, N. Velisavljevic, M. Wilke, C.-S. Yoo, C. Baehtz, U. Zastrau, and C. Strohm, "Novel experimental setup for megahertz x-ray diffraction in a diamond anvil cell at the high energy density (hed) instrument of the european x-ray free-electron laser (euxfel)." J Synchrotron Radiat. **28 Pt 3**, 688–706 (2021).

[15] C. Multiphysics, "Introduction to comsol multiphysics®," COMSOL Multiphysics, Burlington, MA, accessed Feb **9**, 2018 (1998).

[16] A. J. Campbell, L. Danielson, K. Righter, C. T. Seagle, Y. Wang, and V. B. Prakapenka, "High pressure effects on the iron–iron oxide and nickel–nickel oxide oxygen fugacity buffers," Earth and Planetary Science Letters **286**, 556–564 (2009).

[17] F. Farah, K. K. M. Lee, and M. C. Akin, "Temperature distribution in a laser-heated diamond anvil cell as described by finite element analysis," AIP Advances **12**, 105218 (2022), https://doi.org/10.1063/5.0094377.

[18] J.-P. Poirier, "Light elements in the earth's outer core: A critical review," Physics of the Earth and Planetary Interiors **85**, 319–337 (1994).

[19] U. Zastrau, K. Appel, C. Baehtz, O. Baehr, L. Batchelor, A. Berghäuser, M. Banjafar, E. Brambrink, V. Cerantola, T. E. Cowan, *et al.*, "The high energy density scientific instrument at the european xfel," Journal of synchrotron radiation **28**, 1393–1416 (2021).

[20] H.-P. Liermann, H. Damker, Z. Konôpková, K. Appel, A. Schropp, S. McWiliams, A. Goncharov, and C. Baehtz, "Conceptual design report for diamond anvil cell setup (dac) at the hed instrument of the european xfel," (2016).

[21] Y. Fei and Y. Wang, "High-pressure and high-temperature powder diffraction," Reviews in Mineralogy and Geochemistry **41**, 521–557 (2000).

[22] R. Boehler and K. D. Hantsetters, "New anvil designs in diamond-cells," High Pressure Research **24**, 391 – 396 (2004).

[23] C. Prescher and V. B. Prakapenka, "Dioptas: a program for reduction of two-dimensional x-ray diffraction data and data exploration," High Pressure Research **35**, 223–230 (2015).

[24] S. Tateno, T. Komabayashi, K. Hirose, N. Hirao, and Y. Ohishi, "Static compression of b2 kcl to 230 gpa and its pvt equation of state," American Mineralogist: Journal of Earth and Planetary Materials **104**, 718–723 (2019).

[25] A. Dewaele, A. Belonoshko, G. Garbarino, F. Occelli, P. Bouvier, M. Hanfland, and M. Mezouar, "High-pressure–high-temperature equation of state of kcl and kbr," Phys. Rev. B **85** (2012), 10.1103/PhysRevB.85.214105.

[26] O. Ball, C. Prescher, K. Appel, C. Baehtz, M. Baron, R. Briggs, V. Cerantola, J. Chantel, S. Chariton, A. Coleman, *et al.*, "Dynamic optical spec-

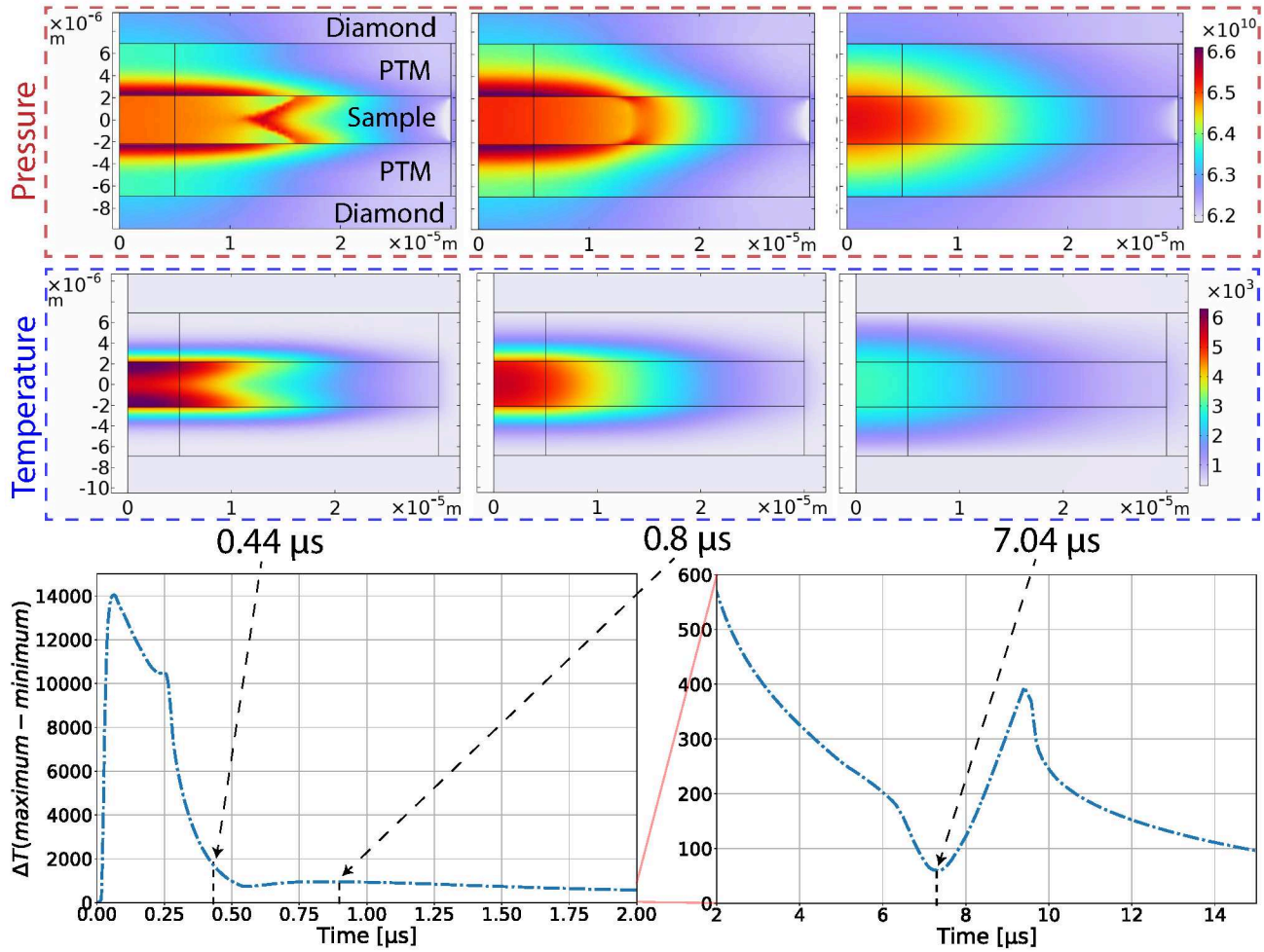

FIG. 14. Top and middle three figures respectively model's total pressure (P_{ref}+ +P_{th}) and temperature maps at t=0.44, 0.88 and 7.04 µs (from left to right). For the model reproducing run # 414. Pressure map shows reduced pressure within molten zones of the sample compared to solid ones, in agreement with the shear modulus drop upon melting. Bottom graphs: temperature difference between minimum and maximum temperature within X-ray sampled zone vs time (divided into two figures due to the huge temperature gradient differences vs time). This emphasizes µs-scale temperature homogenization occurring in the sample.

troscopy and pyrometry of static targets under optical and x-ray laser heating at the european xfel," Journal of Applied Physics **134** (2023).

[27]Z. Konôpková, R. S. McWilliams, N. Gómez-Pérez, and A. F. Goncharov, "Direct measurement of thermal conductivity in solid iron at planetary core conditions," Nature **534**, 99–101 (2016).

[28]J. Meza-Galvez, N. Gomez Perez, A. Marshall, A. Coleman, K. Appel, H.-P. Liermann, M. Mcmahon, Z. Konôpková, and R. McWilliams, "Thermo-mechanical response of thickly tamped targets and diamond anvil cells under pulsed hard x-ray irradiation," Journal of Applied Physics **127**, 195902 (2020).

[29]H. Hwang, T. Kim, H. Cynn, T. Vogt, R. J. Husband, K. Appel, C. Baehtz, O. B. Ball, M. A. Baron, R. Briggs, M. Bykov, E. Bykova, V. Cerantola, J. Chantel, A. L. Coleman, D. Dattlebaum, L. E. Dresselhaus-Marais, J. H. Eggert, L. Ehm, W. J. Evans, G. Fiquet, M. Frost, K. Glazyrin, A. F. Goncharov, Z. Jenei, J. Kim, Z. Konôpková, J. Mainberger, M. Makita, H. Marquardt, E. E. McBride, J. D. McHardy, S. Merkel, G. Morard, E. F. I. O'Bannon, C. Otzen, E. J. Pace, A. Pelka, C. M. Pépin, J. S. Pigott, V. B. Prakapenka, C. Prescher, R. Redmer, S. Speziale, G. Spiekermann, C. Strohm, B. T. Sturtevant, N. Velisavljevic, M. Wilke, C.-S. Yoo, U. Zastrau, H.-P. Liermann, M. I. McMahon, R. S. McWilliams, and Y. Lee, "X-ray free electron laser-induced synthesis of epsilon-iron nitride at high pressures," The Journal of Physical Chemistry Letters **12**, 3246–3252 (2021), pMID: 33764078, https://doi.org/10.1021/acs.jpclett.1c00150.

[30]D. Greiffenberg, "The agipd detector for the european xfel," Journal of Instrumentation **7**, C01103 (2012).

[31]A. Allahgholi, J. Becker, A. Delfs, R. Dinapoli, P. Goettlicher, D. Greiffenberg, B. Henrich, H. Hirsemann, M. Kuhn, R. Klanner, A. Klyuev, H. Krueger, S. Lange, T. Laurus, A. Marras, D. Mezza, A. Mozzanica, M. Niemann, J. Poehlsen, J. Schwandt, I. Sheviakov, X. Shi, S. Smoljanin, L. Steffen, J. Sztuk-Dambietz, U. Trunk, Q. Xia, M. Zeribi, J. Zhang, M. Zimmer, B. Schmitt, and H. Graafsma, "The Adaptive Gain Integrating Pixel Detector at the European XFEL," Journal of Synchrotron Radiation **26**, 74–82 (2019).

[32]P. Saha and G. D. Mukherjee, "Thermal conductivity of iron and nickel during melting: Implication to the planetary liquid outer core," Pramana **97**, 1 (2022).

[33]S. Merkel, R. J. Hemley, and H.-k. Mao, "Finite-element modeling of diamond deformation at multimegabar pressures," Applied Physics Letters **74**, 656–658 (1999).

[34]A. Dewaele, G. Fiquet, and P. Gillet, "Temperature and pressure distribution in the laser-heated diamond–anvil cell," Review of scientific instruments **69**, 2421–2426 (1998).

[35]C. E. Yen, Q. Williams, and M. Kunz, "Thermal pressure in the laser-heated diamond anvil cell: A quantitative study and implications for the density versus mineralogy correlation of the mantle," Journal of Geophysical Research: Solid Earth **125**, e2020JB020006 (2020).

[36]F. Miozzi, J. Matas, N. Guignot, J. Badro, J. Siebert, and G. Fiquet, "A new reference for the thermal equation of state of iron," Minerals **10**, 100 (2020).
[37]N. Tsujino, Y. Nishihara, Y. Nakajima, E. Takahashi, K.-i. Funakoshi, and Y. Higo, "Equation of state of γ-fe: Reference density for planetary cores," Earth and Planetary Science Letters **375**, 244–253 (2013).
[38]Y. Kuwayama, G. Morard, Y. Nakajima, K. Hirose, A. Q. R. Baron, S. I. Kawaguchi, T. Tsuchiya, D. Ishikawa, N. Hirao, and Y. Ohishi, "Equation of state of liquid iron under extreme conditions," Phys. Rev. Lett. **124**, 165701 (2020).
[39]G. Morard, G. Garbarino, D. Andrault, D. Antonangeli, N. Guignot, J. Siebert, M. Roberge, E. Boulard, A. Lincot, A. Denoeud, *et al.*, "Density measurements and structural properties of liquid and amorphous metals under high pressure studied by in situ x-ray scattering," in *AGU Fall Meeting Abstracts*, Vol. 2013 (2013) pp. MR44A–06.
[40]M. Hass, J. A. Harrington, D. A. Gregory, and J. W. Davisson, "Infrared absorption limits of hf and df laser windows," Applied Physics Letters **28**, 610–611 (1976), https://doi.org/10.1063/1.88584.
[41]S. Webster, Y. Chen, G. Turri, A. Bennett, B. Wickham, and M. Bass, "Intrinsic and extrinsic absorption of chemical vapor deposition single-crystal diamond from the middle ultraviolet to the far infrared," JOSA B **32**, 479–484 (2015).
[42]A. Savvatimskiy and S. Onufriev, "Specific heat of liquid iron from the melting point to the boiling point," High Temperature **56**, 933–935 (2018).
[43]C. D. Chliatzou, M. J. Assael, K. D. Antoniadis, M. L. Huber, and W. A. Wakeham, "Reference correlations for the thermal conductivity of 13 inorganic molten salts," Journal of Physical and Chemical Reference Data **47**, 033104 (2018), https://doi.org/10.1063/1.5052343.
[44]A. Kirshenbaum, J. Cahill, P. McGonigal, and A. Grosse, "The density of liquid nacl and kcl and an estimate of their critical constants together with those of the other alkali halides," Journal of Inorganic and Nuclear Chemistry **24**, 1287–1296 (1962).
[45]C. A. Klein and G. F. Cardinale, "Young's modulus and poisson's ratio of cvd diamond," Diamond and Related Materials **2**, 918–923 (1993), diamond 1992.
[46]A. Rajabpour, L. Seidabadi, and M. Soltanpour, "Calculating the bulk modulus of iron and steel using equilibrium molecular dynamics simulation," Procedia Materials Science **11**, 391–396 (2015).
[47]T. Kinoshita, T. Mashimo, and K. Kawamura, "The mechanism and effect of defects in the b1–b2 phase transition of kcl under high pressure: molecular dynamics simulation," Journal of Physics: Condensed Matter **17**, 1027 (2005).
[48]C. Authors and editors of the volumes III/17A-22A-41A1a, "Diamond (c) bulk modulus," Group IV Elements, IV-IV and III-V Compounds. Part a-Lattice Properties , 1–9 (2001).
[49]S. S. Lobanov and Z. M. Geballe, "Non-isotropic contraction and expansion of samples in diamond anvil cells: Implications for thermal conductivity at the core-mantle boundary," Geophysical Research Letters **49**, e2022GL100379 (2022), e2022GL100379 2022GL100379, https://agupubs.onlinelibrary.wiley.com/doi/pdf/10.1029/2022GL100379.
[50]R. S. McWilliams, D. A. Dalton, Z. Konôpková, M. F. Mahmood, and A. F. Goncharov, "Opacity and conductivity measurements in noble gases at conditions of planetary and stellar interiors," Proceedings of the National Academy of Sciences **112**, 7925–7930 (2015).
[51]E. Edmund, G. Morard, M. A. Baron, A. Rivoldini, S. Yokoo, S. Boccato, K. Hirose, A. Pakhomova, and D. Antonangeli, "The fe-fesi phase diagram at mercury's core conditions," Nature Communications **13**, 387 (2022).
[52]D. Andrault, L. Pison, G. Morard, G. Garbarino, M. Mezouar, M. A. Bouhifd, and T. Kawamoto, "Comment on: Melting behavior of SiO_2 up to 120 GPa (Andrault et al. 2020)," Physics and Chemistry of Minerals **49**, 3 (2022).
[53]A. Gleason, C. Bolme, H. Lee, B. Nagler, E. Galtier, D. Milathianaki, J. Hawreliak, R. Kraus, J. Eggert, D. Fratanduono, *et al.*, "Ultrafast visualization of crystallization and grain growth in shock-compressed sio2," Nature communications **6**, 8191 (2015).
[54]A. Gleason, C. Bolme, H. Lee, B. Nagler, E. Galtier, R. Kraus, R. Sandberg, W. Yang, F. Langenhorst, and W. Mao, "Time-resolved diffraction of shock-released sio2 and diaplectic glass formation," Nature communications **8**, 1481 (2017).
[55]R. A. Fischer, A. J. Campbell, D. M. Reaman, N. A. Miller, D. L. Heinz, P. Dera, and V. B. Prakapenka, "Phase relations in the fe–fesi system at high pressures and temperatures," Earth and Planetary Science Letters **373**, 54–64 (2013).
[56]A. Krygier, M. Harmand, B. Albertazzi, E. E. McBride, K. Miyanishi, D. Antonangeli, Y. Inubushi, R. Kodama, M. Koenig, T. Matsuoka, G. Mogni, F. Pietrucci, A. M. Saitta, T. Togashi, Y. Umeda, T. Vinci, M. Yabashi, T. Yabuuchi, G. Fiquet, and N. Ozaki, "X-ray diffraction study of phase transformation dynamics of fe and fe-si alloys along the shock hugoniot using an x-ray free electron laser," Phys. Rev. B **105**, L220102 (2022).
[57]Y. Mori, H. Ozawa, K. Hirose, R. Sinmyo, S. Tateno, G. Morard, and Y. Ohishi, "Melting experiments on fe–fe3s system to 254 gpa," Earth and Planetary Science Letters **464**, 135–141 (2017).
[58]G. Morard, D. Andrault, D. Antonangeli, Y. Nakajima, A. Auzende, E. Boulard, S. Cervera, A. Clark, O. Lord, J. Siebert, *et al.*, "Fe–feo and fe–fe3c melting relations at earth's core–mantle boundary conditions: Implications for a volatile-rich or oxygen-rich core," Earth and Planetary Science Letters **473**, 94–103 (2017).
[59]J. Li, Q. Wu, J. Li, T. Xue, Y. Tan, X. Zhou, Y. Zhang, Z. Xiong, Z. Gao, and T. Sekine, "Shock melting curve of iron: A consensus on the temperature at the earth's inner core boundary," Geophysical Research Letters **47**, e2020GL087758 (2020).
[60]D. Zhou, J. Dong, Y. Si, F. Zhu, and J. Li, "Melting curve of potassium chloride from in situ ionic conduction measurements," Minerals **10**, 250 (2020).
[61]T. Komabayashi, "Thermodynamics of melting relations in the system fe-feo at high pressure: Implications for oxygen in the earth's core," Journal of Geophysical Research: Solid Earth **119**, 4164–4177 (2014).
[62]J.-P. Poirier, *Earth's Interior - second edition* (Cambridge University Press, 2008).
[63]A. C. Hindmarsh, P. N. Brown, K. E. Grant, S. L. Lee, R. Serban, D. E. Shumaker, and C. S. Woodward, "Sundials: Suite of nonlinear and differential/algebraic equation solvers," ACM Transactions on Mathematical Software (TOMS) **31**, 363–396 (2005).
[64]O. Schenk and K. Gärtner, "Solving unsymmetric sparse systems of linear equations with pardiso," Future Generation Computer Systems **20**, 475–487 (2004).